


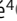





ARTICLE

Local glycolysis fuels actomyosin contraction during axonal retraction

Renata Santos^{1,2} , Ludmilla Lokmane³ , Dersu Ozdemir¹ , Clément Traoré⁴ , Annabelle Agesilas⁴, Coralie Hakibilen⁴ , Zsolt Lenkei^{1,4,5*} , and Diana Zala^{1,4*} 

In response to repulsive cues, axonal growth cones can quickly retract. This requires the prompt activity of contractile actomyosin, which is formed by the non-muscle myosin II (NMII) bound to actin filaments. NMII is a molecular motor that provides the necessary mechanical force at the expense of ATP. Here, we report that this process is energetically coupled to glycolysis and is independent of cellular ATP levels. Induction of axonal retraction requires simultaneous generation of ATP by glycolysis, as shown by chemical inhibition and genetic knock-down of GAPDH. Co-immunoprecipitation and proximal-ligation assay showed that actomyosin associates with ATP-generating glycolytic enzymes and that this association is strongly enhanced during retraction. Using microfluidics, we confirmed that the energetic coupling between glycolysis and actomyosin necessary for axonal retraction is localized to the growth cone and near axonal shaft. These results indicate a tight coupling between on-demand energy production by glycolysis and energy consumption by actomyosin contraction suggesting a function of glycolysis in axonal guidance.

Introduction

Brain wiring is an essential developmental process in which neurons project axons that connect to their proper target to form functional circuits. Axonal guidance is mediated by a complex orchestration of attractive and repulsive cues that drive the growth cone to its final destination (Lokmane and Garel, 2014; Chédotal and Richards, 2010). The physiological importance of this developmental process is highlighted by several neurological disorders characterized by aberrant neuronal connections (Van Battum et al., 2015). Several mutations in genes involved in axonal guidance have indeed been found in human neurological disorders (Engle, 2010; Van Battum et al., 2015). In addition, non-genetic factors such as inflammation, maternal stress, or prenatal drug exposition can also lead to aberrant neuronal connectivity (Tortoriello et al., 2014; Lautarescu et al., 2020; Rasmussen et al., 2019).

Growth cones at the tip of the axons are dynamic structures that express receptors for the guidance cues, which for the main part are chemotrophic factors that induce growth toward or away from the source, such as the secreted netrins and slits or the membrane-bound ephrins and semaphorins (Ye et al., 2019; Seiradake et al., 2016; Blockus and Chédotal, 2016). Other factors

have been identified that contribute to the complexity of axonal guidance and brain wiring. For example, cannabinoids and lysolipids function as repulsive cues that induce growth cone collapse and retraction of the axon (Gaffuri et al., 2012; Berghuis et al., 2007; Mulder et al., 2008; Saez et al., 2020; Wu et al., 2010; Ye et al., 2019; Guy and Kamiguchi, 2021; Quarta et al., 2017; Roland et al., 2014). Guidance factors activate several signaling pathways that cause cytoskeletal and membrane remodeling, resulting in an array of morphological changes, such as growth, arrest, collapse, retraction, turning, or branching. This motility of the growth cone is possible through the dynamic F-actin networks and myosin motors that allow mechanotransduction of the signals necessary for axonal pathfinding (McCormick and Gup-ton, 2020). Therefore, the shape of the growth cones is diverse and depends on the type of neurons, developmental stage, and environment; it can range from a simple single thin filopodium to a sizable display of filopodia and lamellipodia (Ye et al., 2019).

The endocannabinoid system is involved in axonal fasciculation and guidance by chemorepulsion of axonal growth cones during corticogenesis (Gaffuri et al., 2012; Berghuis et al., 2007;

¹Université Paris Cité, Institute of Psychiatry and Neuroscience of Paris, INSERM U1266, Laboratory of Dynamics of Neuronal Structure in Health and Disease, Paris, France; ²Institut des Sciences Biologiques, Centre national de la recherche scientifique, Paris, France; ³Institut de Biologie de l'Ecole Normale Supérieure, École Normale Supérieure, Centre national de la recherche scientifique, Paris Sciences et Lettres Research University, Paris, France; ⁴Brain Plasticity Unit, École Supérieure de Physique et de Chimie Industrielles-ParisTech, Paris, France; ⁵GHU-Paris Psychiatrie et Neurosciences, Hôpital Sainte Anne, Paris, France.

*Z. Lenkei and D. Zala contributed equally to this paper. Correspondence to Diana Zala: diana.zala@inserm.fr; Renata Santos: renata.santos@inserm.fr.

© 2023 Santos et al. This article is distributed under the terms of an Attribution-Noncommercial-Share Alike-No Mirror Sites license for the first six months after the publication date (see <http://www.rupress.org/terms/>). After six months it is available under a Creative Commons License (Attribution-Noncommercial-Share Alike 4.0 International license, as described at <https://creativecommons.org/licenses/by-nc-sa/4.0/>).

Mulder et al., 2008; Saez et al., 2020; Wu et al., 2010). The endocannabinoid 2-arachidonoglycerol (2-AG) is secreted from the subventricular zone (SVZ) and the cortical plate during embryonic development (Maccarrone et al., 2014), which prevents growing corticofugal axons expressing the cannabinoid receptor 1 (CB1) to enter the SVZ from the intermediate zone (Roland et al., 2014). Activation of CB1 at the growth cone activates the Ras homolog gene family member A (RHOA) and the Rho-associated coiled-coil-containing protein kinase (ROCK), resulting in axonal retraction mediated by actomyosin contractility (Berghuis et al., 2007; Roland et al., 2014; Backer et al., 2018). Other cues also induce axonal retraction through the RHOA/ROCK/actomyosin pathway, such as activation of the Eph/ephrin reverse signaling (Takeuchi et al., 2015) or various lysolipids (Quarta et al., 2017; Obara et al., 2011; Zhang et al., 2003). Therefore, the contractile actomyosin complex is a major player in growth cone collapse and retraction, acting downstream of repulsive guidance cues and RHOA/ROCK (Wahl et al., 2000; Wylie and Chantler, 2003; Gallo, 2006; Brown et al., 2009; Murray et al., 2010; Roland et al., 2014).

Non-muscular myosin II (NMII) is the motor component of the actomyosin complex. NMII is formed by three pairs of chains: two heavy chains containing the ATPase catalytic site and the F-actin binding domain, two regulatory light chains (RLCs), and two essential light chains that stabilize the structure (Garrido-Casado et al., 2021). Phosphorylation of RLCs downstream of ROCK causes a change in NMII conformation, self-association into bipolar filaments, and binding to F-actin forming the actomyosin complex. This contractile machinery exerts its mechanical tasks by consuming energy by the NMII ATPase catalytic site (Geeves, 2016). The three isoforms of NMII are expressed in neurons and the axons, but only NMIIA, which is enriched in the shaft and central domain, is thought to be responsible for axonal retraction (Miller and Suter, 2018). Accordingly, it was previously shown that in response to cannabinoids, NMII is phosphorylated, therefore active in the axonal region adjacent to the growth cone (Roland et al., 2014). However, the source of the ATP that fuels NMII contractility and axonal retraction is not known.

Neuronal bioenergetics strongly depends on mitochondrial metabolism (Kim et al., 2019; Yellen, 2018). Despite that, local glycolysis provides ATP for several active processes that require a transient and fast increase in energy (Díaz-García et al., 2017; Ivannikov et al., 2010; Zala et al., 2017; Yellen, 2018). Compared with mitochondrial oxidative phosphorylation, glycolytic enzymes can be localized close to ATP-consuming effectors. Stimulation of neuronal excitability immediately triggers a transient increase in aerobic glycolysis in response to activity of Na⁺/K⁺ pump activity (Díaz-García et al., 2017; Díaz-García and Yellen, 2019; Meyer et al., 2022). Also, a tight coupling between ATP production by glycolytic enzymes and consumption occurs for processive motors, such as kinesin and dynein for fast axonal transport of vesicles (Zala et al., 2013; Hinckelmann et al., 2016), and for the proton pumps at synaptic vesicles (Ishida et al., 2009; Ikemoto et al., 2003). In these cases, glycolytic enzymes form complexes with the ATP-consuming proteins and ATP is provided by direct channeling without an exchange with the

cytosolic ATP pool. Assembly of proteins participating in the same functional pathway in complexes or super-complexes was selected during evolution and present multiple advantages, such as counteracting the dispersion of enzymes and substrates in the cell and allowing fine regulation of activity (Lyon et al., 2021).

When contractile actomyosin is engaged in axonal retraction, it requires a rapid and continuous supply of ATP. While little is known about the energy source for actomyosin activity, several observations suggest that glycolysis may be associated with contractile forces in various cellular contexts. In 1988, George et al. observed that pharmacological inhibition of glycolysis blocked the shortening of amputated axons (George et al., 1988). Stress fibers, which contain actomyosin, are enriched in the key glycolytic enzyme glyceraldehyde 3-phosphate dehydrogenase (GAPDH; Schmitz and Bereiter-Hahn, 2002), which can bind to F-actin (Waingeh et al., 2006). Other pieces of evidence show that the glycolytic enzyme pyruvate kinase PKM2 phosphorylates NMII during cytokinesis (Jiang et al., 2014) and that the glucose transporter GLUT1 is structurally linked to actomyosin at tight junctions (Salvi et al., 2021). Recently, it was shown that five representative enzymes from the investment and payoff phases of glycolysis are present at the growth cone, mainly in the central domain and filipodia, in sensory neurons (Ketschek et al., 2021). These data indicate a possible functional link between NMII activity and glycolysis, which may provide ATP locally and on demand for actomyosin contractility. The presence and putative importance of such a close coupling has not been demonstrated yet. Therefore, here, we tested this hypothesis and studied the energetic metabolism of actomyosin contraction during axonal retraction.

Results

Glycolysis, but not mitochondrial respiration, is necessary to provide ATP for axonal retraction

Axonal dynamics was monitored in neurons expressing Lifeact-mCherry, which is a red fluorescent probe that binds to F-actin, in a media containing glucose and pyruvate, as previously described (Roland et al., 2014). As expected, addition of the synthetic cannabinoid WIN 55,212-2 (WIN) to growing axons activated CB1-induced growth cone collapse and axonal retraction in <2 min (Fig. 1 A and Fig. S1). We used oligomycin to inhibit the mitochondrial ATP synthase and 2-deoxyglucose (2DG), a non-metabolizable glucose analogue to block glycolysis. While inhibiting mitochondria or glycolysis by addition of oligomycin or 2DG caused growth cone collapse induced by WIN, only 2DG restrained axonal retraction (Fig. 1 A and Fig. S1). Simultaneous addition of oligomycin and 2DG to the medium blocked WIN-induced retraction similarly to 2DG inhibition (Fig. 1 A). These results suggested that only glycolysis is required for axonal retraction induced by WIN. Furthermore, axonal retraction was completely blocked when the assay was performed in neurons incubated for 1 h in media containing pyruvate as a unique energetic substrate, while retraction was normal when incubated for 1 h with glucose (Fig. 1 B). Similar results were obtained by blocking the two metabolic pathways 20 min before inducing axonal retraction and by using additional inhibitors, iodoacetate

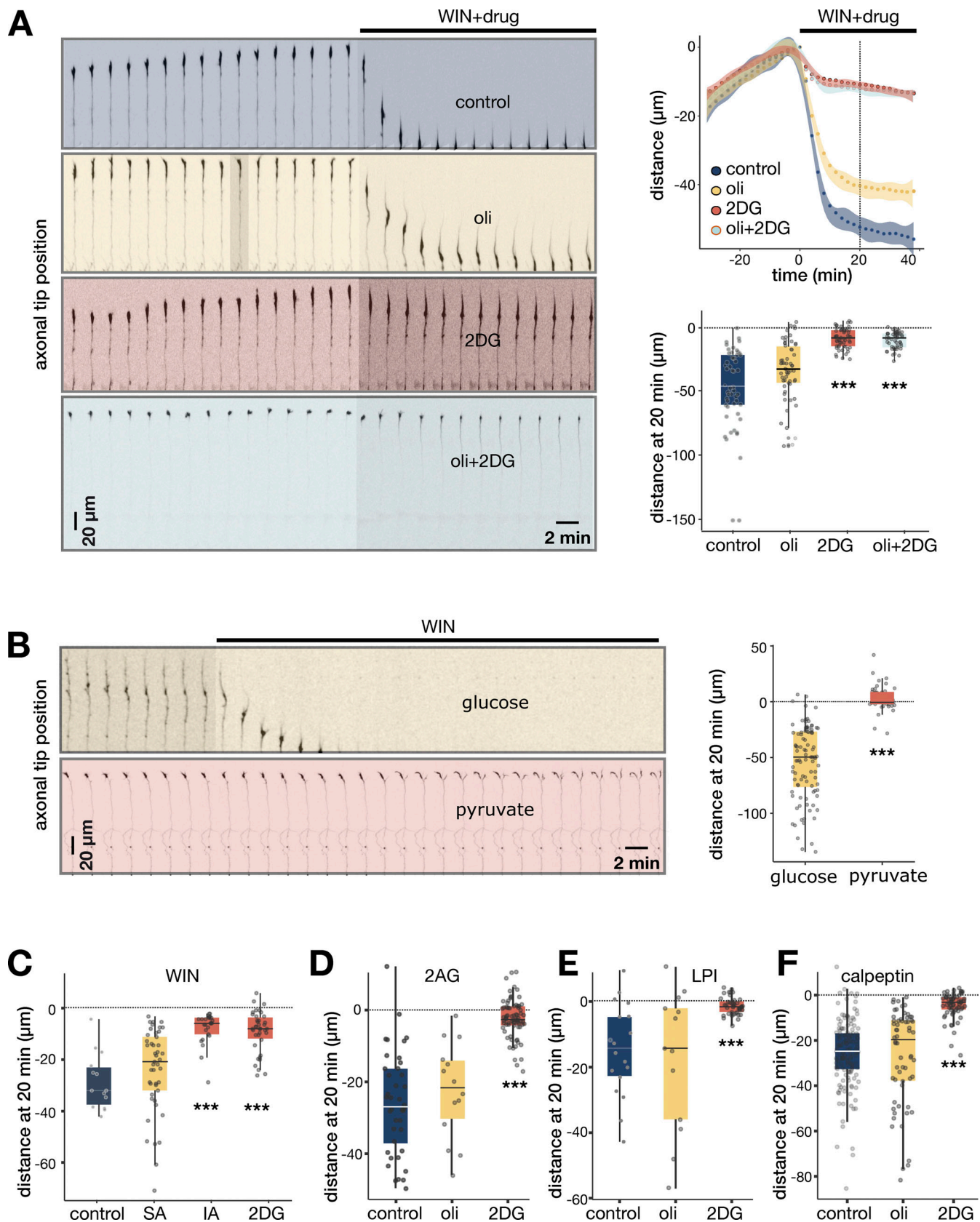


Figure 1. **Glycolysis, but not mitochondrial respiration, is necessary to provide ATP for axonal retraction.** (A) Image series of video-microscopy showing the dynamics of axonal tip position before and during WIN+metabolic drugs exposure in media containing 10 mM glucose and 1 mM pyruvate. Hippocampal neurons expressing LifeAct-mCherry were imaged at a frequency of 0.5 frames/min for 30 min before the induction of retraction. Oligomycin, 2DG, or DMSO

(control) were added in combination with WIN. On the top right is shown the quantification of the position of the growth cone (distance from position relative to time zero corresponding to the injection of WIN). On the bottom right, the boxplot shows values 20 min after drug injections; $51 < n < 58$ axons from three independent experiments. **(B)** Image series of video-microscopy showing the dynamics of axonal tip position before and during WIN exposure in media containing 10 mM glucose or 1 mM pyruvate in hippocampal neurons. On the right, the boxplot shows values 20 min after drug injections; $43 < n < 94$ axons from two independent experiments. **(C)** Boxplot showing values 20 min after WIN injection and 40 min after treatment with DMSO (control; $n = 19$, two independent experiments), 5 mM sodium azide (SA; $n = 30$, three independent experiments), 1 mM iodoacetate (IA; $n = 25$; two independent experiments), or 30 mM 2DG ($n = 38$, two independent experiments) in hippocampal neurons. **(D)** Boxplot showing values 20 min after 1 μ M 2-AG injection in combination with oligomycin (oli), 2DG, or DMSO in hippocampal neurons; $14 < n < 77$ axons from two independent experiments. **(E)** Boxplot showing values 20 min after 2 μ M LPI injection in combination with oligomycin, 2DG, or DMSO in cortical neurons; $13 < n < 41$ axons from two independent experiments. **(F)** Boxplot showing values 20 min after 0.2 U/ml calpeptin in combination with oligomycin, 2DG, or DMSO in cortical neurons; $52 < n < 101$ axons from two independent experiments. For all experiments, cell concentrations of the drugs were 100 nM WIN, 10 μ M oligomycin, and 30 mM 2DG. Statistics: one-way ANOVA followed by Tukey HSD post-test correction; *** $P < 0.001$.

for glycolysis and sodium azide for mitochondrial respiration (Fig. 1 C). The physiological CB1 ligand endocannabinoid 2-AG induced retraction of smaller amplitude compared with WIN, similarly to what was previously described (Roland et al., 2014), but only the addition of 2DG inhibitor blocked axonal retraction (Fig. 1 D). To substantiate these observations, we tested the effects of physiological lysophosphatidylinositol (LPI), the endogenous agonist of G protein-coupled receptor 55 ligand, in cortical neurons and observed comparable results (Fig. 1 E). Finally, we tested direct activation using calpeptin, which activates RHOA downstream of CB1 allowing by-passing the heterogeneity of the receptor expression in neurons after transfection. Again, 2DG, but not oligomycin, blocked axonal retraction (Fig. 1 F). These results show that glycolysis, but not mitochondria, is required for axonal retraction independently of the stimulus.

Cannabinoids and RHOA activation do not affect considerably the energetic metabolism and the local ATP levels

Glycolysis may provide ATP for axonal retraction by two distinct mechanisms: from the cytosolic pool or by local production in a multienzyme complex where the ATP is directly transferred from the ATP-generating glycolytic enzymes to the active site of NMII (Fig. 2 F). To test which mechanism fuels actomyosin contraction in response to cannabinoids in embryonic rat hippocampal cultures, we used a Seahorse analyzer to simultaneously quantify oxygen consumption rate (OCR) and extracellular acidification rate (ECAR), which measure respiration and glycolysis, respectively. As expected, within 5 min we observed a reduction in the OCR with oligomycin treatment and a reduction in the ECAR with 2DG treatment (Fig. 2 A). Analysis of the effects of these two drugs on the total cellular ATP levels for 30 min showed: (1) significant depletion at all time points triggered by oligomycin ($P < 0.01$ or $P < 0.001$, two-way ANOVA); (2) transient change with 2DG, significant compared with the control at 4 min after treatment ($P < 0.01$, two-way ANOVA) but not at 2, 8, 16, and 32 min; and (3) complete consumption after 15 min treatment with the two drugs (Fig. 2 A). This indicated that in the neuronal cultures, the majority of cellular ATP was produced by mitochondria and not by glycolysis and that exhaustion of ATP levels needed inhibition of both metabolic pathways. To gain information on the local subcellular distribution of ATP at the growth cone and the adjacent axonal shaft under metabolic inhibition and axonal retraction, we used the ratiometric ATP/ADP probe Perceval. We have successfully used

this reporter in axons depleted from mitochondria and showed that the sensitivity of this probe was sufficient to monitor metabolic perturbation in small structures (Zala et al., 2013; Hinckelmann et al., 2016). We acquired confocal microscopy images at rest and 2 min after drug treatments of hippocampal neurons transfected with Perceval. Growth cones and adjacent axons were binarized to obtain a mask in which the ratio of ATP to ADP was calculated (Fig. 2 B). As expected, and in agreement with the results of total ATP measures (Fig. 2 A), oligomycin inhibition of mitochondrial ATP generation led to a decrease in ATP and an increase in ADP signals resulting in a decrease of the ATP/ADP ratio at the growth cone and adjacent shaft, which was quantified by the shift of the distribution of pixels towards lower intensities. In contrast, inhibition of glycolysis by 2DG did not affect ATP, ADP signals, or the ratio, resulting in a similar pixel distribution. These results indicate that actomyosin contractility is not correlated with the cytoplasmic ATP/ADP ratio and that glycolysis inhibition does not block actomyosin contractility through modification of ATP levels.

Next, we tested for the impact of cannabinoid signaling on cellular energetic metabolism. Two previous studies reported opposite effects of cannabinoids: an increase in mitochondrial respiration in rat brains and a decrease in mitochondrial respiration and ATP levels in mice brain and primary neurons (Hebert-Chatelain et al., 2016; Costa and Colleoni, 2000). We tested the effect of WIN in human HEK293 cells stably expressing CB1 and observed a reduction of ~10% in mitochondrial respiration and a small but not significant increase in glycolysis at the whole-cell level (Fig. 2 C). Similar results were obtained by treatment of hippocampal neurons with calpeptin (Fig. 2 D). These results show that WIN and calpeptin do not inhibit glycolysis to an extent that could explain the lack of axonal retraction. In addition, they also show the absence of a substantial increase in glycolysis at the whole-cell level, which is in favor of the energetic coupling hypothesis. In addition, calpeptin did not induce a modification of ATP and ADP levels or the ATP/ADP ratio at the growth cone and near the axonal shaft (Fig. 2 E). These data also show that the extent of axonal retraction is not correlated to the total or the local ATP levels (Fig. 1 A and Fig. 2 A). A reduction of 50% in total ATP was observed in the first minutes of oligomycin treatment compared to <10% in ATP with 2DG treatment, but only 2DG inhibited completely axonal retraction. Moreover, a blockade of mitochondrial functions or glycolysis before induction of retraction gave similar results.

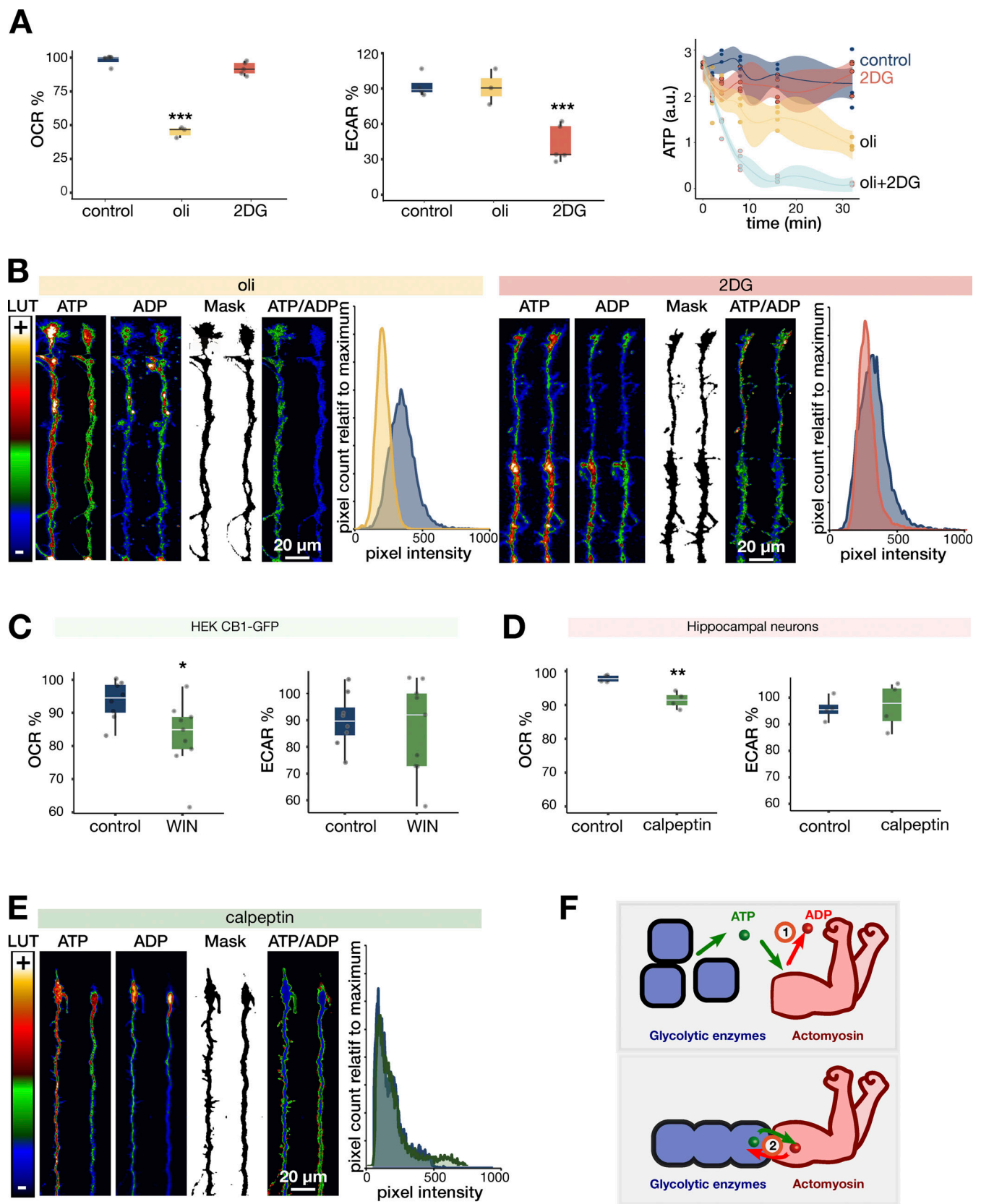


Figure 2. **Cannabinoids and RHOA activation's effect on energetic metabolism and local ATP levels at the growth cone and near axonal shaft.** (A) Box plot showing OCR and ECAR measured in neuronal hippocampal cultures 5 min after injection of 10 μ M oligomycin (oli), 30 mM 2DG, or DMSO (control) using a Seahorse analyzer. Values were normalized to the values measured before injection for each well ($n = 4$). On the right, the evolution of total ATP measured by luminescence after addition of metabolic drugs. Boxplot $n = 4$ (wells). Two-way ANOVA followed by a Bonferroni correction revealed statistical differences in

the oli group as compared with control at 2 min $P < 0.01$, and the following times points $P < 0.001$, in the oli+2DG as compared with control 2 min $P < 0.01$, and the following times points $P < 0.01$, in the 2DG as compared with control at 2 min $P < 0.01$, while no differences were detected at the other time points. **(B and E)** Confocal images of hippocampal growth cones expressing the reporter Perceval before and after 2 min treatment with 10 μ M oligomycin, 30 mM 2DG, or 0.2 U/ml calpeptin. The ATP channel, ADP channel, mask obtained from the ATP channel, and the ATP/ADP ratio calculated inside the mask are shown. LUT: look-up table from the maximum value (+) to the minimal value (-). Histograms with the distribution of ATP/ADP before (blue) and after metabolic inhibition (yellow or red) or calpeptin (green) treatment. **(C)** Boxplot showing OCR and ECAR measured in HEK293 cells stably expressing CBI-eGFP after 5 min of 100 nM WIN injection as in A. Values were normalized to the values measured before injection for each well. $n = 6$ (triplicates, two independent cultures). **(D)** Boxplot showing OCR and ECAR measured in hippocampal neurons after 5 min of 0.2 U/ml calpeptin injection. Values were normalized to the values measured before injection for each well. $n = 4$ (duplicates, two independent cultures). **(F)** Working model of how ATP can be provided to NMII for actomyosin contraction and axonal retraction: (1) by the cytosolic pool or (2) by energetic coupling. Statistics: Student's t test (B and C) or one-way ANOVA followed by Tukey HSD post-test correction (A); * $P < 0.05$. ** $P < 0.01$. *** $P < 0.001$.

Considering these results, we could expect that repulsive cues would induce glycolysis to increase ATP levels necessary for axonal retraction. However, in our conditions, the activation of the CBI/RHOA repulsive pathway slightly reduced mitochondrial respiration but did not significantly affect either global glycolysis rate or local ATP levels. In conclusion, these results show that simultaneous generation of new ATP by glycolysis is necessary to fuel CBI/RHOA-mediated actomyosin contraction and axonal retraction. This is in favor of the second proposed mechanism where new synthesized ATP is directly transferred from glycolytic enzymes to the active site of NMII without exchange with the cytoplasm (Fig. 2 F).

Glycolytic payoff phase enzymes are located at the growth cone during axonal retraction

Glycolysis is a 10-enzyme catabolic pathway from which two enzymes from the investment phase (aldolase and triosephosphate isomerase [TPII]) and three enzymes from the payoff phase (GAPDH, enolase, and pyruvate kinase [PK]) were extensively quantified at the growth cones of sensory neurons (Ketschek et al., 2021; see diagram in Fig. S2). The ATP-producing payoff phase comprises five enzymes. The key enzymes are GAPDH, which is the first enzyme and frequently used as a surrogate marker for the entire pathway, and phosphoglycerate kinase (PGK) and PK, which catalyze the reactions that generate ATP. We performed a retraction assay using hippocampal neurons that expressed GAPDH-eGFP to follow the distribution and dynamics of GAPDH (Fig. 3 A and Video 1). We observed the presence of GAPDH-eGFP at the growth cone and distal axon during the growth phase, collapse, and retraction, which colocalized with F-actin (visualized by Lifeact-mCherry). This localization was confirmed by confocal microscopy on endogenous GAPDH and F-actin (Fig. 3 B). We showed previously that induction of retraction increased the amount of phosphorylated RLC in the axonal shaft (Roland et al., 2014). Therefore, we investigated the colocalization of NMII, GAPDH, and PGK with F-actin, which is enriched at the growth cone, and with microtubules, which are present in the axonal shaft and the central domain of the growth cone. For this, hippocampal cultures were treated for 5 min with DMSO (control or growth conditions) or calpeptin (retraction conditions; Fig. 3 C), fixed, and processed for immunofluorescence. NMII was enriched in the central and transition domains of the growth cone and in the axonal shaft in control and retraction conditions. GAPDH and PGK shared the same localization, colocalizing with actin at the

growth cone and with microtubules in the axonal shaft (Fig. 3 C). Next, we asked if the remaining three enzymes of the payoff phase (phosphoglycerate mutase, enolase, and PK) were also present at the growth cone and adjacent axonal shaft and colocalized with F-actin. Indeed, all enzymes colocalized with F-actin and were detected at the growth cone and adjacent axonal shaft both in growth and retraction conditions (Fig. 3 C and Fig. S2). In summary, the five enzymes of the payoff phase of glycolysis are located at the growth cone and adjacent axonal shaft and colocalize with F-actin during axonal retraction.

GAPDH is necessary for axonal retraction

To confirm the requirement of glycolysis for axonal retraction, we used RNA interference to reduce expression of GAPDH and consequently, to impair the downstream steps of glycolysis, which are responsible for ATP production. We tested the efficacy of two different small interfering RNAs (siRNAs) in decreasing GAPDH expression at the growth cone. For this, hippocampal neurons were cotransfected with siRNA (against GAPDH or a universal control) and a plasmid expressing LifeAct-mCherry for visualization of transfected growth cones, fixed, and immunostained with an anti-GAPDH antibody. GAPDH expression was evaluated by measuring the mean fluorescence intensity at the growth cone region defined by F-actin, as detected by LifeAct-mCherry fluorescence (Fig. 4 A). A significant drop but not a full extinction in GAPDH signal intensity was detected with both siRNA-GAPDH as compared with control siRNA, indicating a decrease in GAPDH expression (Fig. 4 B). Next, we tested the effect of siRNAs in the axonal retraction assay and observed a significant reduction in the amplitude of retraction with the two siRNA-GAPDH as compared with the control siRNA (Fig. 4, C and D). The partial effect of siRNAs relative to drug inhibition may be the result of residual GAPDH expression as detected in Fig. 4, A and B. Interestingly, the siRNA had also an effect on the axonal growth (Fig. 4, C and E). These results show that GAPDH expression at the growth cone and near shaft is necessary for axonal retraction.

Glycolytic enzymes dynamically associate with actomyosin during axonal retraction

Having shown that axonal retraction required glycolytic enzymes, we asked if these enzymes could form a molecular complex with NMII, which is the molecular motor and ATPase of actomyosin. Therefore, we performed NMII immunoprecipitation using an antibody that recognizes NMII heavy chains from

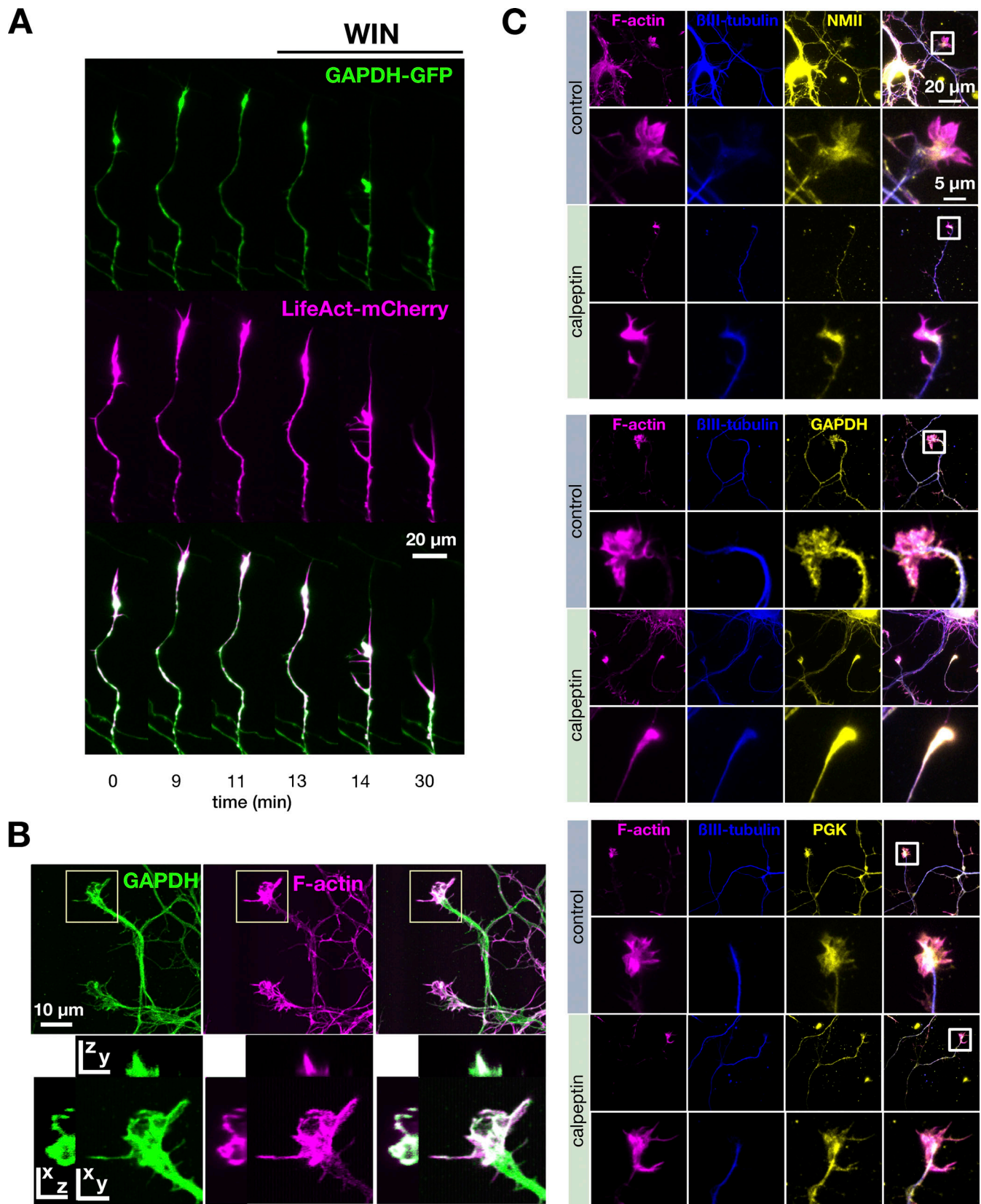


Figure 3. **Glycolytic payoff phase enzymes are located at the growth cone during axonal retraction.** (A) Time-lapse images of a hippocampal growth cone and adjacent axonal shaft expressing Lifeact-mCherry (magenta) and GAPDH-eGFP (green) during growth and 100 nM WIN-induced axonal retraction (related to Video 1). (B) Confocal images of hippocampal neurons immunostained for endogenous GAPDH (green) and phalloidin (magenta). Below is shown an enlargement of the growth cone with the orthogonal views. (C) Immunofluorescence images of hippocampal neurons, and enlarged images in growth and retraction.

conditions (control, DMSO) or after 2-min-induced retraction by 0.2 U/ml calpeptin. F-actin staining with phalloidin shown in magenta; microtubules detected with β III-tubulin shown in blue, and NMII, GAPDH, and PGK shown in yellow. Growth cones are recognizable by their characteristic morphology with the phalloidin staining in magenta.

protein extracts prepared from cortical cultures. Unsupervised analysis by mass spectrometry (MS) of proteins from NMII and GFP precipitate revealed 450 putative NMII-interacting proteins from 1,435 identified (Table S1). These proteins were selected based on a peptide sequencing coverage over 10% of the sequence, a higher peak area, and a higher NMII specificity (i.e., abundance in NMII precipitate as compared to GFP precipitate). Interestingly, glycolysis was in the top 10 functional terms identified by Gene Ontology (GO) analysis that were enriched in this data (Tables 1 and S1). As expected, heavy and light chains of NMII and actin were the most abundant proteins detected and increased by hundreds of fold in magnitude in NMII precipitate compared with GFP precipitate (Tables 2 and S1). Interestingly, effectors of CB1/RHOA/ROCK signaling and axonal guidance were specifically pulled-down with NMII (Tables 2 and S1). Two glycolytic enzymes of the investment phase (glucose-6-phosphate isomerase and TPII, the fifth and last enzyme of this phase) and five of the payoff phase were also identified as putative NMII interactors by MS (Tables 2 and S1), and confirmed by western blot for GAPDH and the two ATP-producing enzymes, PGK and PK (Fig. 5 A). This suggests that production of ATP may occur locally, in a molecular complex, to fuel NMII activity and actomyosin contraction.

To visualize this putative complex in neurons, we used the proximity ligation assay (PLA), which detects two proteins at <40 nm distance, suggesting direct protein–protein interaction (Fredriksson et al., 2002; Alam, 2018). Glycolytic enzymes and actin are abundant proteins; furthermore, actin is present as monomers (G-actin) or polymers (F-actin) in the cell. Therefore, to visualize the proteins specifically associated with the cytoskeleton, neurons were permeabilized with detergent before fixation to wash out all unbound cytoplasmic proteins and keep intact F-actin, and microtubules and their associated proteins were stabilized by phalloidin and taxol. NMII-actin was detected close to F-actin in basal conditions and, as expected, the PLA signal increased significantly after a 5-min treatment with calpeptin (Fig. 5, B and D), indicating the formation of the actomyosin complex. GAPDH-actin was also proximal to actin and, similarly to NMII, recruitment of GAPDH to F-actin was increased by calpeptin treatment (Fig. 5, B and D). This increase was specific to actin cytoskeleton as PLA fluorescence signal between tubulin and GAPDH was not increased by calpeptin (Fig. 5 B). Finally, the couples NMII-GAPDH and NMII-PGK were also observed in close proximity in basal conditions and, most interestingly, a large increase was observed in both PLA fluorescence signals following calpeptin treatment (Fig. 5, B and D). To quantify the localization of this putative association at the growth cone and adjacent axonal shaft, we represented the position of the PLA NMII-PGK punctae relative to the distal tip (Fig. 5 C). Interestingly, the PLA punctae were regularly distributed from the tip of the growth cone to the adjacent shaft, with a mean of 8.7 μ m from the axonal tip corresponding to the

proximal part of the growth cone. This localization is consistent with the localization of phosphorylated NMII previously described during axonal retraction (Roland et al., 2014). In other terms, recruitment of GAPDH and PGK to NMII and F-actin was enhanced at the growth cone and adjacent axonal shaft under retraction conditions. Altogether, these results suggest the formation of a glycolytic-actomyosin complex during axonal retraction.

Local glycolysis is required for axonal retraction

To test the hypothesis that glycolysis is required locally to power axonal retraction, we took advantage of microfluidic devices to isolate axonal growth cones from dendrites and cell bodies (Taylor et al., 2005). The polydimethylsiloxane (PDMS) microchip (Fig. 6 A) consists of two chambers (Fig. 6, A 1 and 3) that are connected by long channels (Fig. 6, A 2) in which axons can extend from the proximal chamber to the distal chamber. To prevent the diffusion of drugs from the growth cone and adjacent axonal shaft to the rest of the axons and cell bodies, we created a pressure gradient by reducing the volume of media in the distal chamber. This was confirmed by the injection of fluorescein in the distal chamber and absence of leakage into the microchannels (Fig. 6 B). Video microscopy was performed when axons started to grow into the distal chamber (Fig. 6, A 3). Axonal retraction was induced by injection of LPI in the distal chamber (Fig. 6 C). Inhibition of axonal retraction was observed when glycolysis was simultaneously blocked by 2DG injection in the growth cone chamber, but not by 2DG injection in the somatic chamber (Fig. 6 C). These results show that local glycolysis is required for axonal retraction. Altogether, our results support the model of energetic coupling between glycolytic enzymes and actomyosin contractility (Fig. 6 D).

Discussion

Here, we investigated how energy was supplied to NMII, a processive motor that converts ATP into mechanical forces used for actomyosin contractility. We found, using complementary approaches, that glycolytic enzymes and actomyosin form a dynamic functional complex necessary for axonal retraction in response to physiological ligands (endocannabinoids and LPI). Using microfluidics, we confirmed that this energetic coupling between glycolysis and actomyosin is localized to the region encompassing the growth cone and near axonal shaft, which is consistent with the localization of phosphorylated NMII previously described during axonal retraction (Roland et al., 2014). This type of energetic coupling, where ATP is produced locally and on demand, was described before for other dynamic neuronal functions that need an instant and high supply of ATP (Kim et al., 2019; Zala et al., 2017; Yellen, 2018). These results contribute to the accumulating evidence showing that essential functions of a neuronal cell, such as firing (Díaz-García et al.,

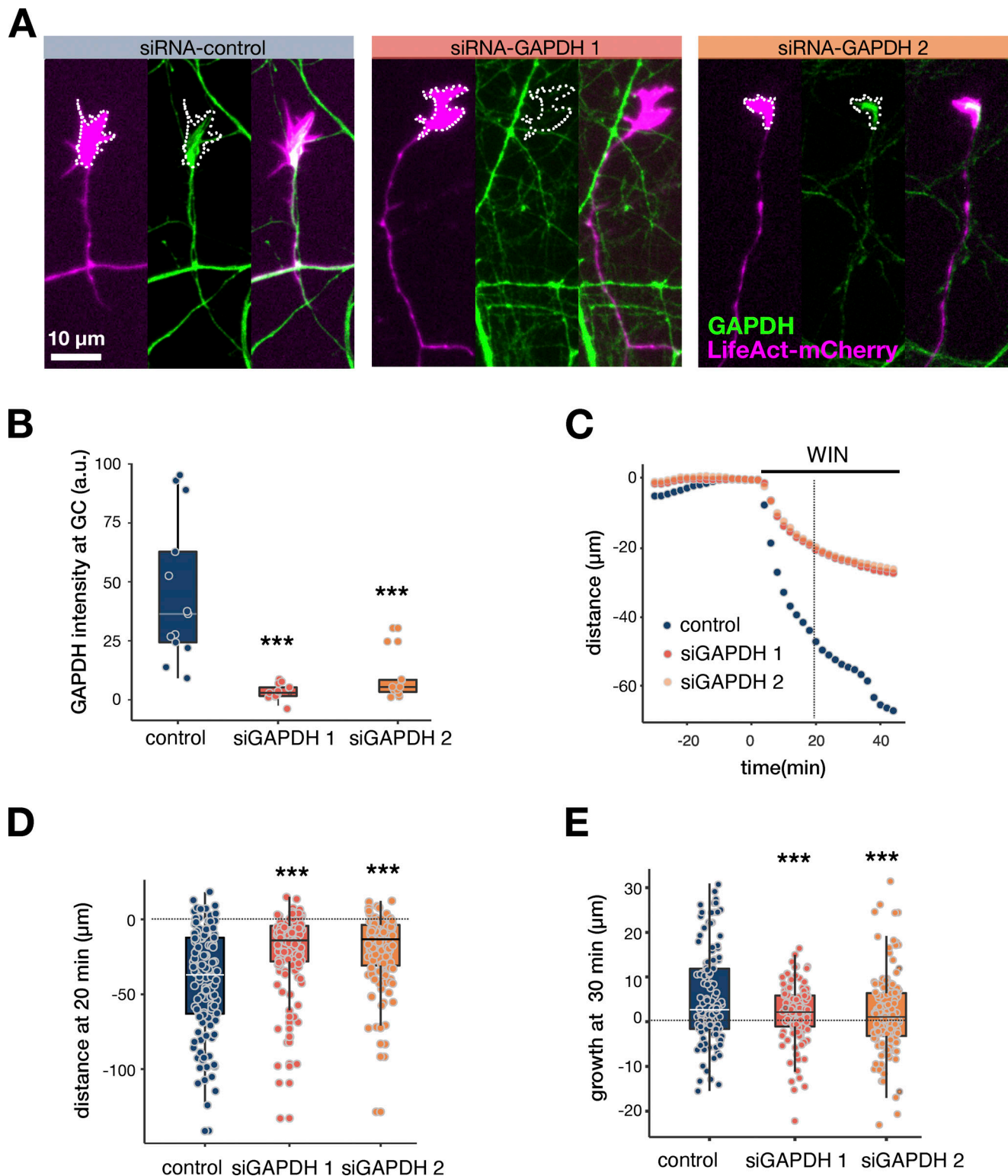


Figure 4. GAPDH is necessary for axonal retraction. (A) Endogenous GAPDH expression was detected by immunostaining (in green) at the growth cone and adjacent axonal shaft in hippocampal neurons cotransfected with siRNAs and LifeAct-mCherry (in magenta) for F-actin visualization and as a transfection control. The outline of the growth cones was drawn (white dashed lines) on the LifeAct-mCherry channel. (B) Boxplot showing GAPDH intensity at individual growth cones (GC). Mean intensity of GAPDH was measured on the region defined by LifeAct-mCherry fluorescence, as shown in A; $36 < n < 55$ axons from two independent experiments. (C) WIN (100 nM)-induced axonal retraction assay showing the average distance from position at the beginning of the experiment. $36 < n < 97$ axons from three independent experiments. (D and E) Boxplot showing the distance of the growth cone at 20 min after WIN induction as well as after 30 min growth; $36 < n < 97$ axons from three independent experiments. Statistics: one-way ANOVA followed by Tukey honestly significant difference (HSD) post-test correction; *** $P < 0.001$.

Table 1. **Top 10 functional categories of putative NMII-interacting proteins (complete data in Table S1)**

GO biological process	List total	List IP	Expected	Fold enrichment	P value
Regulation of modification of postsynaptic structure (GO:0099159)	14	7	0.29	23.98	1.22E-03
NADH regeneration (GO:0006735)	15	7	0.31	22.38	1.76E-03
Glucose catabolic process to pyruvate (GO:0061718)	15	7	0.31	22.38	1.76E-03
Canonical glycolysis (GO:0061621)	15	7	0.31	22.38	1.76E-03
ARP2/3 complex-mediated actin nucleation (GO:0034314)	15	7	0.31	22.38	1.76E-03
RAB protein signal transduction (GO:0032482)	18	8	0.38	21.32	3.06E-04
Postsynaptic actin cytoskeleton organization (GO:0098974)	21	9	0.44	20.56	5.30E-05
Glycolytic process through glucose-6-phosphate (GO:0061620)	17	7	0.35	19.75	3.44E-03
Glycolytic process through fructose-6-phosphate (GO:0061615)	17	7	0.35	19.75	3.44E-03
Postsynaptic cytoskeleton organization (GO:0099188)	23	9	0.48	18.77	1.00E-04

2017; Ivannikov et al., 2010; Ikemoto et al., 2003; Ishida et al., 2009), axonal transport of vesicles (Zala et al., 2013), and as shown here, retraction of processes, require simultaneous breakdown of glucose by glycolysis, the cellular pool of mitochondrial ATP not being consumed.

During brain development, the precise arrangement of neuronal connections is established by neurite and axonal outgrowth and retraction. Retraction of axons occurs during development to eliminate improperly addressed or supernumerary projections, or in the adult in case of injury (Cowan

Table 2. **NMII-interacting proteins identified by MS (complete data in Table S1)**

Function	Protein	Description	Accession number (SwissProt)	% coverage	% NMII enrichment ^a
Myosin (actomyosin)	MYH10	Myosin-10 (NMIIB)	Q9JLT0	58.81	97.71
	MYH9	Myosin-9 (NMIIA)	Q62812	48.09	98.71
	MYL6	Myosin light chain 6	Q64119	58.28	97.36
	MYL9	Myosin RLC 9	Q64122	33.92	100
	RLC-A	Myosin RLC RLC-A	P13832	50.58	100
Actin (actomyosin)	ACTB	Actin, cytoplasmic 1	P60711	85.87	100
	ACTG1	Actin, cytoplasmic 2	P63259	85.87	100
CB1/RHOA/ROCK signaling	CNRP1	CB1 cannabinoid receptor-interacting protein 1	Q5M7A7	16.46	100
	RHOA	Transforming protein RHOA	P61589	10.36	100
	MPRIIP	Myosin phosphatase Rho-interacting protein	Q9ERE6	42.95	100
	ROCK1	Rho-associated protein kinase 1	Q63644	1.24	100
	ROCK2	Rho-associated protein kinase 2	Q62868	4.18	100
Axonal guidance	SRGAP2	SLIT-ROBO Rho GTPase-activating protein 2	D4A208	13.54	100
	TRIO	Triple functional domain protein	F1M0Z1	8.00	98.86
Glycolysis (investment phase)	GPI	Glucose-6-phosphate isomerase	Q6P6V0	12.37	100
	TPI1	Triosephosphate isomerase	P48500	31.73	48.23
Glycolysis (payoff phase)	GAPDH	Glyceraldehyde-3-phosphate dehydrogenase	P04797	41.44	44.26
	PGK1	Phosphoglycerate kinase 1	P16617	39.81	84.60
	PGAM1	Phosphoglycerate mutase 1	P25113	33.46	100
	PGAM2	Phosphoglycerate mutase 2	P16290	8.30	100
	ENO1	Enolase	P04764	34.56	7.82
	PKM	Pyruvate kinase	P11980	38.04	59.99

^a(NMII area – GFP area)/NMII area.

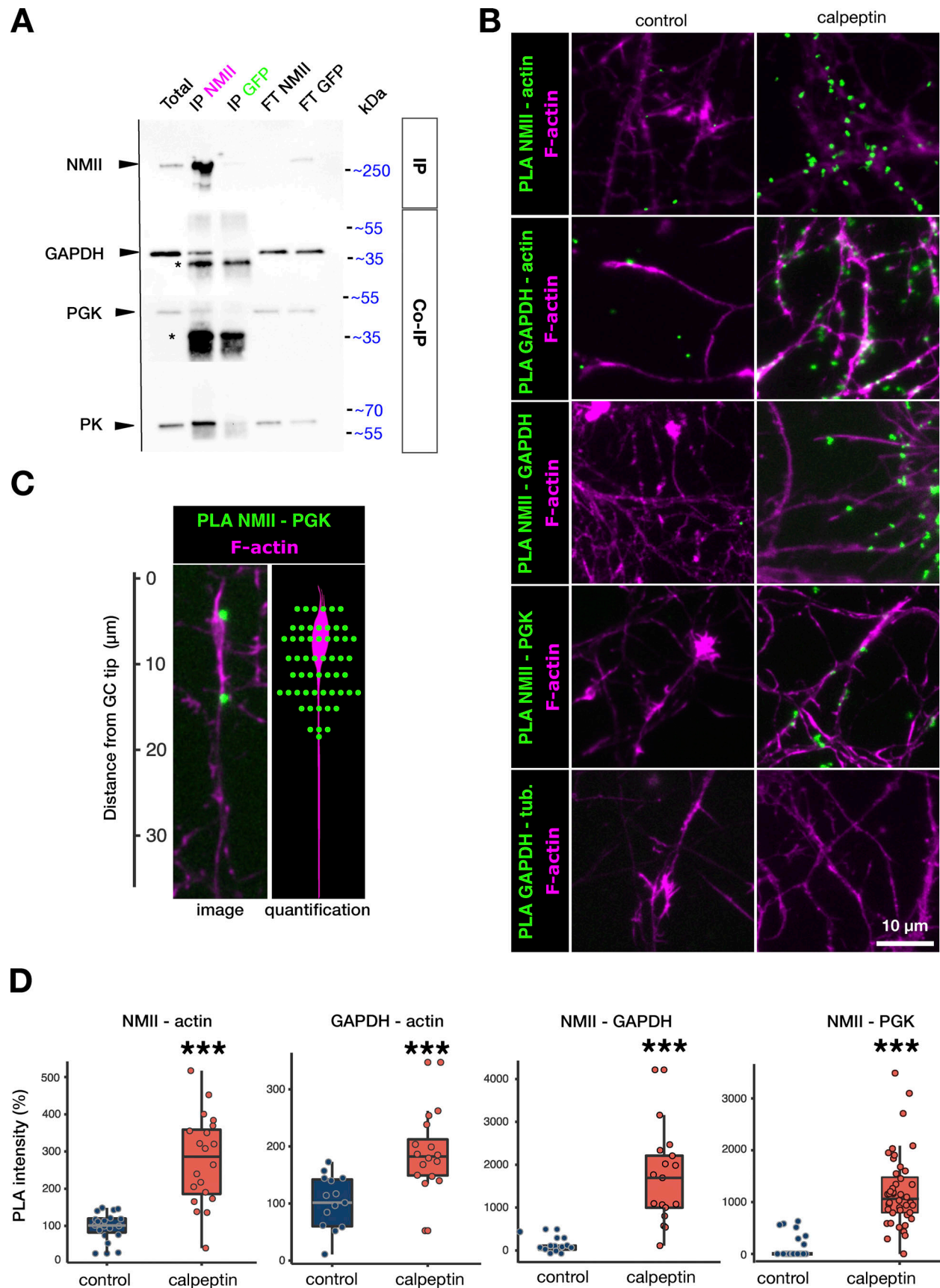


Figure 5. **Glycolytic enzymes dynamically associate with actomyosin during axonal retraction.** (A) Western blot showing co-immunoprecipitation (co-IP) of NMII and the glycolytic enzymes GAPDH, PGK, and PK from protein extracts of rat cortical neuronal cultures at DIV3. IgGs are marked by *.

(B) Fluorescence images of PLA (in green) and phalloidin staining (in magenta) of the couples of proteins: NMII (phosphorylated RLC) and actin; GAPDH and actin; NMII (heavy chain) and GAPDH; NMII (heavy chain) and PGK; and GAPDH and tubulin. **(C)** Fluorescence image example with two PLA NMII-PGK punctae and quantification of the position relative to the tip of the growth cone (GC) of 56 PLA NMII-PGK in 26 isolated GCs of calpeptin-treated neurons. **(D)** Boxplot of PLA signal intensity of neurites of hippocampal neurons treated for 5 min with DMSO (control) or 0.2 U/ml calpeptin of two independent experiments. Statistics: Student's *t* test; ****P* < 0.001.

et al., 1984; Pease and Segal, 2014; Gan and Lichtman, 1998; Luo and O'Leary, 2005). Growth cone pathfinding at the tip of axons is a succession of phases of growth, pause, collapse, retraction, and bifurcation (Dumoulin et al., 2021; Wen and Zheng, 2006). It is recognized that mitochondria are required for axonal growth and branching (Courchet et al., 2013; Smith and Gallo, 2018). However, it was recently found that glycolytic enzymes are localized at the growing cone and that glycolysis is necessary for sensory axonal extension (Ketschek et al., 2021; Courchet et al., 2013). This requirement for glycolysis may result from a more efficient energy channeling compared with mitochondria, resulting from a higher rate of ATP production due to the physical proximity of ATP production (Pfeiffer et al., 2001). Therefore, glycolysis could play a more important role in growth cone dynamics than previously assumed.

Physical interaction between glycolytic enzymes and the cytoskeleton has been known for 40 yr (Knoll and Walsh, 1992; Shearwin et al., 1990; Masters, 1984), but its physiological significance may have been masked by the abundance of these proteins. Cytoskeleton architecture and contractility are essential for cellular division, migration, and differentiation. These are energy-demanding processes, and it is likely that the required ATP is provided by a functional interaction with glycolytic enzymes, as reported here. In agreement with this idea, a recent study showed that energy production by aerobic glycolysis in normal and cancer cells is regulated in response to the mechanical properties of the environment, which is sensed by the actomyosin cytoskeleton (Park et al., 2020). Activation of the RHOA/ROCK signaling pathway by multiple signals and receptors results in actomyosin contractility and cytoskeleton remodeling (Amano et al., 2010; Narumiya and Thumkeo, 2018; Amin et al., 2013). A number of these signals and effectors that activate RHOA, for example, ephrins and trio rho guanine nucleotide exchange factor (TRIO), are also implicated in axonal guidance (Backer et al., 2018; Shamah et al., 2001; Wahl et al., 2000). Also, several studies showed that a long-term activation of RHOA and ROCK induces glucose uptake and glycolysis (Wu et al., 2021; Yang et al., 2016; Begum et al., 2002; Furukawa et al., 2005). Therefore, an exciting hypothesis is that RHOA/ROCK may be a key hub that simultaneously triggers rapid energy-consuming structural changes and direct channeling of ATP generated by glycolysis. Interestingly, we found that several of these proteins interact with NMII by MS analysis.

Glycolytic enzymes can be associated in transient complexes by protein-protein interactions to form supramolecular complexes, allowing an efficient substrate channeling or tunneling (Zhang and Fernie, 2021; Sweetlove and Fernie, 2018). In our specific case, there are two potential mechanisms that could explain how glycolytic enzymes are recruited to the actomyosin complex. GAPDH and PGK interact with F-actin but also with the

monomeric β -actin (Havugimana et al., 2022; Go et al., 2021; Waingeh et al., 2006; Schmitz and Bereiter-Hahn, 2002). RHOA induces the formation of the actomyosin complex, which involves the activation of NMII and the assembly of actin filaments. Therefore, one possible mechanism is the hijacking of glycolytic enzymes by actin during F-actin polymerization. A second possible mechanism could involve post-translational modifications of glycolytic enzymes. Many post-translational modifications of GAPDH have been identified, which play a fundamental role in the diverse cellular functions of this moonlighting protein (Sirover, 2020, 2021).

One of the current hypotheses for the emergence of neurodevelopmental disorders is dysfunctional brain energetic metabolism (Oyarzábal et al., 2021; Kim et al., 2019). Therefore, understanding how energy is generated and consumed during axonal navigation can help predict the effect of defects in glycolysis or mitochondrial ATP in brain connectivity. We and others observed that blocking the endocannabinoid system by the specific CB1 receptor antagonist/inverse agonist AM281 by RHOA knockout or the NMII inhibitor blebbistatin affected axonal guidance with an increased number of misrouted axons in the SVZ (Roland et al., 2014; Cappello et al., 2012). We expect that a similar effect would be observed by decreasing glycolysis during embryonic development.

In conclusion, in this study, we presented evidence that a higher-order complex actomyosin-glycolysis at the growth cone is necessary for the translation of the repulsive signal of endocannabinoids or LPI and activation of RHOA into axonal retraction (Fig. 6 D). The ATP necessary for NMII contraction is generated directly on demand by the glycolytic enzymes associated with actomyosin.

Materials and methods

Cell cultures

Human embryonic kidney cells (HEK293, RRID:CVCL_0045, from CRL-1573; ATCC) stably expressing FLAG-CB1-GFP (Leterrier et al., 2006) were cultivated in DMEM (Thermo Fisher Scientific) with 10% FBS (Thermo Fisher Scientific). Hippocampal and cortical neuronal cultures were derived from combined male and female rat embryos at embryonic day 18 (E18; Sprague Dawley, RRID:RGD_734476, from Janvier Labs). The different brain structures were dissected in cold DMEM (Thermo Fisher Scientific) under a stereomicroscope and tissue was dissociated enzymatically in HBSS (Thermo Fisher Scientific) with trypsin (0.1%; Sigma-Aldrich) and DNase I (0.001%; Roche) for 15 min at 37°C. Trypsin was inactivated by addition of trypsin inhibitor (0.1%; Thermo Fisher Scientific). The cells were dissociated by delicate trituration with a pipette tip and the resulting suspension was centrifuged. The cells were

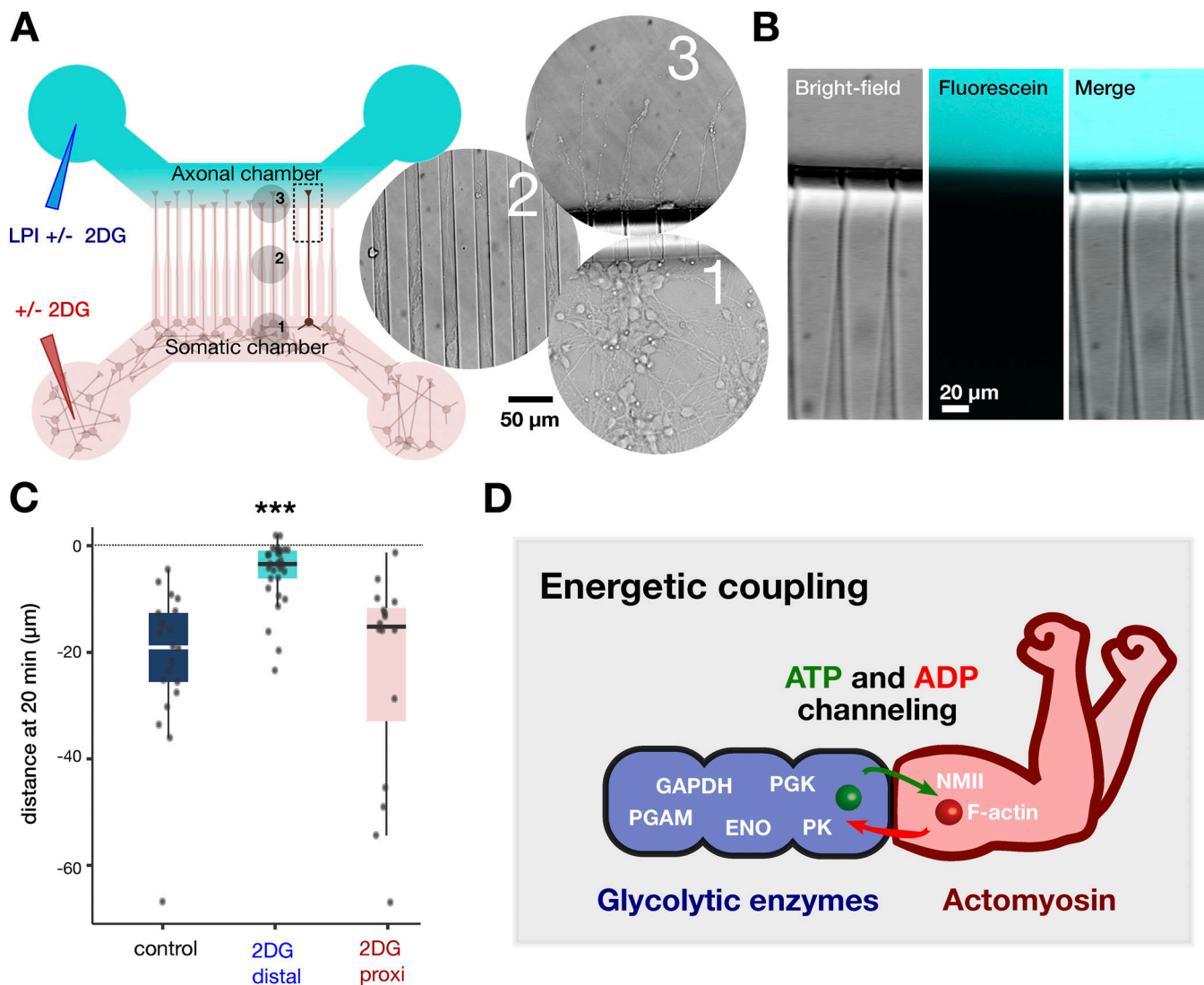


Figure 6. Local glycolysis is required for axonal retraction. (A) On the left, a schematic representation of the PDMS-based microfluidic devices and experimental design used for local application of drugs at the distal compartment (in blue; LPI plus or minus 2DG) or at the proximal somatic compartment (in light red; plus or minus 2DG). The two compartments are connected by small channels in which axons extend from the proximal compartment to reach the distal chamber. On the right, bright-field images of the three compartments: (1) somatic chamber containing the cortical neuronal cell bodies; (2) channels for axonal extension; and (3) distal axonal chamber with axonal tips that have exited the channels. (B) Bright-field and fluorescence images after 15 min of fluorescein injection in the growth cone chamber. Due to a pressure gradient, fluorescein does not diffuse into the axonal channels. (C) Axonal retraction assay was performed when growth cones reached the distal growth cone chamber (DIV4–7). Video microscopy was performed in bright-field at a frequency of 1 frame/minute for 15 min before the induction of retraction by LPI injection at the distal chamber. For the local inhibition test, 2DG was injected with LPI in the axonal chamber (2DG distal) or the 2DG was injected in the somatic compartment simultaneously with LPI injection in the growth cone chamber (2DG proxi). Boxplot showing values of axonal retraction 20 min after LPI injection (control: $n = 21$, three independent experiments; 2DG distal $n = 30$, three independent experiments; 2DG proxi $n = 16$, two independent experiments). Statistics: one-way ANOVA followed by Tukey HSD post-test correction; *** $P < 0.001$. (D) Proposed model of axonal retraction fueling by energetic coupling between actomyosin and glycolysis. The ATP that fuels NMII contraction and axonal retraction is generated locally and on demand by the glycolytic enzymes associated with actomyosin.

resuspended in neurobasal media (Thermo Fisher Scientific) supplemented with 2% B-27 (Thermo Fisher Scientific), 1% penicillin/streptomycin (Thermo Fisher Scientific), and 2 mM L-glutamine (GlutaMAX, Thermo Fisher Scientific; NB+ media), and plated on the required surface previously coated with poly-D-lysine. Cortical neuronal cultures were kept in this media. For hippocampal neuronal cultures, media was changed after a period of 2 h to allow attachment to NB+ media conditioned for 24 h on a rat glial culture (NB+C

media). Cultures were kept in a humidified incubator (95% air, 5% CO_2) at 37°C.

Plasmid and siRNA transfection

Neuronal cultures were transfected between days in vitro (DIV) 4 and DIV8 with lipofectamine 2000 (Thermo Fisher Scientific) as previously described (Roland et al., 2014). Plasmids used were: GAPDH-eGFP (Dastoor and Dreyer, 2001), CB1-CFP (Roland et al., 2014), Lifeact-mCherry (Riedl et al., 2008; Roland

et al., 2014), and Perceval (Berg et al., 2009). siRNA targeting sequences were rat GAPDH (1) 5'-CGUAUCGGACGCCUGGUA-3', rat GAPDH (2) 5'-CUUCUCUGGAAUACCAUCA-3', or Universal Negative Control #1 (guaranteeing a minimal reduction of 75%; Sigma-Aldrich).

Axonal retraction assays

Hippocampal neurons were plated in poly-D-lysine (Sigma-Aldrich) coated 18-mm coverslips in 12-well plates at a density of 50,000 cells per well and transfected with lipofectamine 2000 at DIV5–7, which corresponds to 2–3 d previous to axonal retraction assay. The coverslips were mounted in a Ludin chamber with prewarmed modified E4 medium containing glucose (Sigma-Aldrich) and/or pyruvate (Thermo Fisher Scientific; Roland et al., 2014). The chamber was placed in a microscope-incubator set at 37°C and time-lapse video-microscopy on 25–40 LifeAct-mCherry-positive growth cones was recorded with an inverted microscope (NikonN-STORM microscope [Nikon Instruments] equipped with an Ixon DU-897 camera [Andor] and controlled with NIS-Elements) at a frequency of 1 image/min with 20× objective lens plus an additional 1.5 magnification lens for quantification analysis. The drugs injected during the acquisition were calpeptin (Cytoskeleton, Inc.), WIN 55,212-2 (Tocris), 2-AG (Tocris), LPI (Sigma-Aldrich), oligomycin (Sigma-Aldrich), and 2DG (Sigma-Aldrich). For localization of GAPDH-eGFP during retraction, videos were acquired with a 100× objective. Compounds were injected during acquisitions and blind analyses of the videos were performed with Fiji (RRID:SCR_002285; Schindelin et al., 2012). Stacks were first corrected for movement with a stabilizer plug-in (https://www.cs.cmu.edu/~kangli/code/Image_Stabilizer.html) and growth cone dynamics were analyzed with the KymoToolbox plug-in (Zala et al., 2013) and manual tracking.

Microfluidic devices

Microchips composed of a piece of elastomer (PDMS) sealed on Flurodish Tissue Culture Dish with Cover Glass Bottom were manufactured and assembled according to previously published protocol (Taylor et al., 2005), with the difference that the channels connecting the two chambers were designed as diodes (Peyrin et al., 2011; Fig. 6 A). The PDMS resin and the curing agent were manually mixed in a mass ratio of 9:1, poured on the epoxy replicates, and placed in a vacuum chuck for 30–45 min to remove all air bubbles. The polymerization was achieved in an oven at 70°C for at least 2 h. The PDMS was then removed and cut with a scalpel to the dimensions of the glass slide. Four holes were perforated over the reservoirs with a 2-mm puncher. PDMS pieces with the motif pattern faced up and the open Petri dishes were introduced in an O₂ plasma cleaner to activate the PDMS and glass surface. Thereafter, the two surfaces were bound together by exercising a gentle pressure with forceps on the PDMS pieces in the Petri dishes. The chambers and channels were then immediately coated with a mix of poly-D-lysine (0.5 mg/ml) and laminin (10 mg/ml), incubated 3 h at 37°C, and washed three times with neurobasal medium for 10 min. 1 million cortical neurons in 10 µl neurobasal medium were plated in the distal chambers. After 2 h, when neurons have

attached to the surface, neurobasal + B27 was added to the four reservoirs. Cultures were regularly checked between DIV4 and DIV7 to select the microchambers that had at least five axons entering the distal chamber for retraction assay. Prior to the assay and video recording, 20 µl of media was removed from the reservoir of the distal chamber to produce a gradient of pressure between the two chambers, thus preventing drugs from diffusing into the different channels. This was tested by injection of 10 µl of PBS containing fluorescein (~0.02 g/L). Retraction assay was performed by adding 10 µl of 10 µM LPI in the growth cone chamber simultaneously to 150 mM 2DG in the same injection if required or simultaneously to 10 µl of 150 mM 2DG injection in the somatic chamber. Due to the dead volume of the reservoirs and chambers, the final concentration is estimated to be 2–5 µM for LPI and 30–75 mM for 2DG.

ATP measurement and metabolic analyzer assay

For ATP measurement, hippocampal neurons were plated in 96-well plates with black borders seeded at 5,000 cells per well. At DIV7, the neurons were treated with 10 µM oligomycin (Sigma-Aldrich) and 30 mM 2DG (Sigma-Aldrich), CellTiter-Glo (Promega) was added, and photons were measured with a luminometer. For local ATP/ADP measurement, hippocampal neurons were transfected with Perceval and observed at DIV6–7 with a confocal Leica SP8 equipped with a 63× (NA1.4) oil immersion objective. Before acquisition, neurons were incubated for 30 min with 10 µM of the pH reporter SNARF-5F (Thermo Fisher Scientific). For Perceval signal measurement, excitation was set at 405 nm (ADP sensitive) and 496 nm (ATP sensitive) and detection of photomultiplier tube (PMT) detector was set at 520–560 nm. For pH, signal excitation was set at 550 nm and PMT was set at 575–585 nm for the isosbestic record and 615–635 nm for the pH-sensitive signal. pH calibration was acquired at pH 7.0, 7.2, 7.4, 7.6, and 7.8 pH with 10 µM Nigericin (Sigma-Aldrich) after Perceval acquisition. No change in pH was observed between baseline and after drug treatment, therefore no correction was applied in Perceval images.

Acidification rate (proportional to glycolysis) and OCR (respiration) were analyzed using a Seahorse XF analyzer (XFp; Proteogene/Agilent). For this, HEK293 cells were plated at 10,000 cells per well and hippocampal neurons were plated at 5,000 per well (XFp cell culture miniplates; Proteogene/Agilent) and analyzed 1 d after plating or at DIV5–7, respectively. Neuronal media were changed to XF Base Medium (Proteogene/Agilent) at pH 7.4 containing 10 M glucose (Sigma-Aldrich), 1.0 mM pyruvate (Thermo Fisher Scientific), and 0.5 mM glutamine (Sigma-Aldrich). Oligomycin (10 µM; Sigma-Aldrich), 2DG (30 mM; Sigma-Aldrich), WIN (100 nM; Tocris), calpeptin (0.2 U/ml, Cytoskeleton), and control DMSO (Sigma-Aldrich) were loaded at a port of the sensor cartridge (XFp extracellular flux cartridges; Proteogene/Agilent). OCR and ECAR were first measured for 30 min to establish the baseline and 5 min after drug injection. Values represent the percentage of baseline.

Immunofluorescence and PLA staining

For immunofluorescence, hippocampal neurons plated at 50,000 cells per well in 12-well plates (DIV5) were washed with

warm PBS and fixed at room temperature with a warm solution of PBS containing 4% PFA (Sigma-Aldrich) and 4% sucrose (VWR) for 10 min. Cells were washed twice with PBS and blocked for 1 h in a PBS solution containing 1% BSA and 0.1% Triton X-100 followed by 1 h incubation in the blocking solution containing the primary antibodies (1:200). Antibodies used were rabbit monoclonal anti-enolase-2, anti-PGAM1, anti-PKM1/2 anti-PKM2 and anti-GAPDH (Cell Signaling Technology), rabbit polyclonal anti-GAPDH (Sigma-Aldrich), and rabbit monoclonal anti-PGK1 (Abcam). Cells were washed three times with PBS (Thermo Fisher Scientific) and incubated 1 h with fluorescent secondary goat antibodies (1:200), ATTO484-phalloidin (1:200; Sigma-Aldrich). Coverslips were mounted with fluorodish (Sigma-Aldrich) on a glass support before three washes with PBS for 10 min.

For PLA staining, a permeabilization step was performed before fixation to remove the soluble proteins not bound to F-actin and microtubule cytoskeleton before applying the PLA protocol (Duolink in situ PLA; Sigma-Aldrich). Cells were quickly washed with warm PBS and incubated for 3 min in warm extraction solution (1% Triton X-100, 2% polyethylene glycol [MW 35 kD; Sigma-Aldrich]), 2 mM unlabeled phalloidin (Sigma-Aldrich), and 2 mM taxol (Sigma-Aldrich) in PEM buffer (100 mM PIPES, pH 6.9; 1 mM EGTA; 1 mM $MgCl_2$; Sigma-Aldrich). Cells were washed with a warm PEM buffer containing 2 mM unlabeled phalloidin and 2 mM taxol and fixed with a warm solution of 4% PFA and 4% sucrose in PEM buffer. Antibody used was 1:200, mouse monoclonal anti-actin and anti- β -tubulin (EnCor), rabbit polyclonal anti-phospho-myosin (RLC; Rockland), human anti-NMII (Institut Curie), rabbit anti GAPDH (Sigma-Aldrich), and mouse monoclonal anti-PGK1 (Abcam). Incubation with ATTO484-phalloidin (1:1,000; Sigma-Aldrich; for 10 min) was done after the PLA protocol and just before the coverslip mounting.

Protein extraction and co-immunoprecipitation

10 million cortical neurons were plated in 10-cm Petri dishes coated with poly-D-lysine (Sigma-Aldrich). At DIV3, neuronal media was removed, cells were washed with PBS and lysed with 1 ml of buffer containing 20 mM Tris-Cl (pH 7.4), 100 mM NaCl, 1% Triton X-100, 1 mM DTT, 10 mM EDTA, and 1% Halt Protease & Phosphatase Inhibitor Cocktail (Thermo Fisher Scientific). Protein concentration was measured using BCA Protein Assay (Thermo Fisher Scientific). Immunoprecipitation was performed with 1 mg of total proteins in 1 ml and with Dynabeads Protein G coupled with human antibodies anti-NMII or anti-GFP (Institut Curie). Western immunoblotting was performed following standard procedures using 4–20% Mini-PROTEAN TGX Stain-Free Protein Gels and Trans-Blot Turbo Mini 0.2 μ m polyvinylidene fluoride (PVDF) Transfer Packs membranes (Biorad). Primary antibodies for mouse anti-GAPDH (1:1,000; Cell Signaling Technology), rabbit anti-NMII (1:1,000; Institut Curie), rabbit anti-PGK1 (1:1,000; Abcam), and rabbit anti-PKM/2 (1:1,000; Cell Signaling Technology) were incubated overnight at 4°C or 1 h at room temperature. Horse anti-mouse or goat anti-rabbit HRP-coupled secondary antibodies (1:2,500; Cell Signaling Technology) were added (1 h at room temperature) and detected sequentially using SuperSignal West Pico

PLUS Chemiluminescent Substrate luminescence solution (Thermo Fisher Scientific) as per the manufacturer's instructions, and signal was detected with ChemiDoc Touch Imaging System (Biorad).

Liquid chromatography–mass spectrometry (LC-MS/MS) analysis

The magnetic beads were resuspended in 20 μ l of 50 mM NH_4HCO_3 and digested overnight at 37°C with 0.5 μ g trypsin (Promega). The supernatants were dried in a speed vacuum and dissolved in 0.1% formic acid for LC-MS/MS analysis. 200 ng of samples were analyzed on a timsTOF Pro 2 mass spectrometer (Bruker Daltonics) coupled to an Evosep one system (Evosep) operating with the 30SPD method developed by the manufacturer. Briefly, the method is based on a 44-min gradient with a C18 analytical column (0.15 \times 150 mm, 1.9 μ m beads) equilibrated at room temperature and operated at a flow rate of 500 nl/min. H_2O /0.1% formic acid (FA) was used as solvent A and acetonitrile/0.1% FA as solvent B. The timsTOF Pro 2 was operated in parallel accumulation-serial fragmentation (PASEF) mode over a 1.3-s cycle time. Mass spectra for MS and MS/MS scans were recorded between 100 and 1,700 m/z. Ion mobility was set to 0.75–1.25 V·s/cm² over a ramp time of 180 ms. Data-dependent acquisition was performed using six PASEF MS/MS scans per cycle with a near 100% duty cycle. Low m/z and singly charged ions were excluded from PASEF precursor selection by applying a filter in the m/z and ion mobility space. The dynamic exclusion was activated and set to 0.8 min, a target value of 16,000 was specified with an intensity threshold of 1,000. Collisional energy was ramped stepwise as a function of ion mobility. Precursor ions for MS/MS analysis were isolated with a 2-D window for m/z < 700 and 3-D for m/z > 700. Singly charged precursor ions were excluded with a polygon filter. MS raw files were analyzed by Peaks Online X software (build 1.6; Bioinformatics Solution, Inc.) using the *Rattus norvegicus* database (SwissProt release 2022_01, 8,147 entries). Parent mass tolerance was set to 20 ppm with fragment mass tolerance of 0.05 D. Specific tryptic cleavage was selected and a maximum of two missed cleavage was authorized. Half of the disulfide bridge was set as a fixed modification, whereas oxidation, acetylation of protein N-termini, and deamidation were set as possible variable modifications. The maximum number of variable modifications per peptide was limited to three. Identifications were filtered based on a 1% false discovery rate threshold at both peptide and protein group levels. The 450 putative NMII-interacting proteins were selected using the following cutoffs and criteria: peptide coverage in NMII precipitate >10%; $-10\lg P > 50$; area of peaks in NMII precipitate >150; area of peaks in NMII precipitate > area in eGFP precipitate; and specificity index NMII > specificity index GFP. The online tools PANTHER Version 14 were used for GO and gene enrichment analyses (Ashburner et al., 2000; Gene Ontology Consortium, 2021; Mi et al., 2019).

Quantification and statistical analysis

Statistical analysis is described in each figure legend and was performed using jamovi software (Version 1.2). Two-tailed

Table 3. **Key resources**

Reagent or Resource	Source	Identifier
<i>Antibodies</i>		
Mouse monoclonal anti-actin	Cat#MCA-5J11; EnCor	RRID:AB_2572218
Rabbit monoclonal anti-enolase-2	Cat#D20H2; Cell Signaling Technology	RRID:AB_2099308
Rabbit monoclonal anti-GAPDH	Cat#D16H11; Cell Signaling Technology	RRID:AB_10622025
Rabbit polyclonal anti-GAPDH	Cat#G9545; Sigma-Aldrich	RRID:AB_796208
Human anti-GFP (recombinant antibody)	Institut Curie	hVHH antiGFP-hFc
Human anti-NMII (SF9; recombinant antibody)	Institut Curie	SF9-hFc2 A-R-H#01
Rabbit anti-NMII (SF9)	Institut Curie	SF9-RFc A-R-R#42
Rabbit monoclonal anti-PGAM1	Cat#D3J9T; Cell Signaling Technology	RRID:AB_2736922
Rabbit monoclonal anti-PGK1 (EPR19057)	Cat#AB199438 or EPR19057; Abcam	N/A
Rabbit monoclonal anti-PKM1/2	Cat#C103A3; Cell Signaling Technology	RRID:AB_2163695
Rabbit monoclonal anti-PKM2	Cat#D78A4; Cell Signaling Technology	RRID:AB_1904096
Rabbit polyclonal anti-phospho-myosin (RLC)	Cat#600-401-416; Rockland	RRID:AB_217940
Mouse monoclonal anti- β -tubulin	Cat#MCA-1B12; EnCor	RRID:AB_2572389
Goat anti-rabbit HRP-linked antibody	Cat#7074; Cell Signaling Technology	RRID:AB_2099233
Horse anti-mouse HRP-linked antibody	Cat#7076; Cell Signaling Technology	RRID:AB_330924
<i>Chemicals, peptides, and recombinant proteins</i>		
Calpeptin	Cytoskeleton, Inc. Sigma-Aldrich	CNO1 C8999
WIN 55,212-2 (WIN)	Tocris	1038
Dulbecco's D phosphate buffered saline 10 \times	Thermo Fisher Scientific (Gibco)	14200-067
Neurobasal medium (1 \times) [–] glutamine	Thermo Fisher Scientific (Gibco)	21103-049
B-27 supplement (50 \times)	Thermo Fisher Scientific (Gibco)	17504-044
Pen Strep (penicillin 10k U/ml streptomycin) 10 mg/ml	Thermo Fisher Scientific (Gibco)	15140-22
Poly-D-lysine hydrobromide	Sigma-Aldrich	P7280
Laminin	Sigma-Aldrich	L2020
GlutaMAX (100X)	Thermo Fisher Scientific (Gibco)	35050-038
D(+)-glucose	Sigma-Aldrich	G7021
Sodium pyruvate 100 mM	Thermo Fisher Scientific (Gibco)	11360070
Oligomycin	Sigma-Aldrich	O4876
2-Deoxy-D-glucose	Sigma-Aldrich	D8375
Lipofectamine 2000	Thermo Fisher Scientific (Invitrogen)	2393037
HBSS 1M	Sigma-Aldrich	H0887
Triton X-100	Sigma-Aldrich	93443-500ML
Albumine bovin fraction V (BSA)	Euromedex	04-100-810-E
Trypsin inhibitor, soybean	Thermo Fisher Scientific (Gibco)	17075-029
DNase I	Roche	04716728001
Trypsin	Sigma-Aldrich	T-6763
Paraformaldehyde	Sigma-Aldrich	P6148
D(+)-saccharose	VWR	27480.294
Fluoroshield histology mounting medium	Sigma-Aldrich	F6182
ATTO488-phalloidin	Sigma-Aldrich	49409
Polyethylene glycol (MW 35 kD)	Sigma-Aldrich	81310
Phalloidin	Sigma-Aldrich	P2141

Table 3. **Key resources (Continued)**

Reagent or Resource	Source	Identifier
Taxol	Sigma-Aldrich	PHL89806
DMEM	Sigma-Aldrich	D2650
Trypsin	Promega	V511B
Halt protease and phosphatase inhibitor cocktail	Thermo Fisher Scientific	#1861281
<i>Critical commercial assays</i>		
CellTiter-Glo luminescent cell viability assay	Promega	G7570
Seahorse XF analyzer	Proteogene/Agilent	XFp
XFp cell culture miniplates and XFp extracellular flux cartridges	Proteogene/Agilent	103025-100 102022-100
Duolink in situ PLA probe anti-human MINUS	Sigma-Aldrich	DUO92021
Duolink in situ PLA probe anti-mouse MINUS	Sigma-Aldrich	DUO92004
Duolink in situ PLA probe anti-mouse PLUS	Sigma-Aldrich	DUO92004
Duolink in situ PLA probe anti-rabbit PLUS	Sigma-Aldrich	DUO82002
Pierce BCA protein assay kit	Thermo Fisher Scientific	23225
<i>Experimental models: Cell models</i>		
HEK293	ATCC CRL-1573	RRID:CVCL_0045
Primary cortical and hippocampal neuronal cultures from E18 rat embryos	Kaech et al. (2012) ; this paper	N/A
<i>Experimental models: Organisms/strains</i>		
Rat: Sprague Dawley	Janvier Labs RN-SD-F	RRID:RGD_734476
<i>Oligonucleotides</i>		
siRNA targeting sequence: rat GAPDH (1) 5'-CGUAUCGGA CGCCUGGUUA-3'	Sigma-Aldrich	SASI_Rn01_0003788
siRNA targeting sequence: rat GAPDH (2) 5'-CUUCUCUCGAAUACCAUCA-3'	Sigma-Aldrich	SASI_Rn02_00261166
siRNA Universal Negative Control #1	Sigma-Aldrich	SIC001-INMOL
<i>Recombinant DNA</i>		
Plasmid: Lifeact-mCherry	Riedl et al. (2008)	https://www.addgene.org/67303/
Plasmid: CB1-CFP	Roland et al. (2014)	N/A
Plasmid: GAPDH-eGFP	Dastoor and Dreyer (2001)	N/A
<i>Software and algorithms</i>		
NIS- Elements AR	Nikon	Version 4.30.01 (Build 1021)
Rstudio	RStudio	R Studio (RRID:SCR_000432) https://www.r-project.org/
Fiji	Schindelin et al. (2012)	Fiji (RRID:SCR_002285) https://imagej.net/Fiji/Downloads
jamovi (Version 1.2)	The jamovi project, 2020	jamovi (RRID:SCR_016142) https://www.jamovi.org
Stabilizer plug-in	https://www.cs.cmu.edu/~kangli/code/Image_Stabilizer.html	ImageJ (RRID:SCR_003070)
Kymo Tool Box plug-in	Zala et al. (2013)	https://github.com/fabricecordelieres/IJ-Plugin_KymoToolBox
GO enrichment analysis (PANTHER Version 14)		GO (RRID:SCR_002811) https://geneontology.org
Peaks online X software	build 1.6, Bioinformatics Solution, Inc	https://www.bioinfor.com/
<i>Rattus norvegicus</i> database	SwissProt release 2022_01, 8,147 entries	https://www.expasy.org
<i>Other</i>		

Table 3. **Key resources (Continued)**

Reagent or Resource	Source	Identifier
4–20% Mini-PROTEAN TGX stain-free protein gels	Biorad	4568095
Trans-Blot Turbo Mini 0.2 µm PVDF transfer packs	Biorad	1704156
SuperSignal West Pico PLUS chemiluminescent substrate	Thermo Fisher Scientific	34579
FluoroDish, tissue culture dish with cover glass bottom	World Precision Instruments, Inc.	FD35-100
SYLGARD 184 silicone elastomer kit	Dow Corning	DC184

unpaired Student's *t* test was used for comparing two groups and one-way ANOVA was used for comparing three or more groups; both were followed by a post-hoc analysis (Tukey and Bonferroni). Data distribution was assumed to be normal but this was not formally tested. $P < 0.05$ was considered to be statistically significant. Statistics and plotting were performed using R Studio or jamovi. All experiments were replicated at least two times; details are found in the legends of the figures.

Ethics

Rat experimental procedures were performed in accordance with the Council of European Union directive of September 22, 2010 (2010/63/UE), and with the French decree of February 1, 2013 (n°2013-118).

Key resources given in Table 3.

Online supplemental material

This manuscript is accompanied by two supplementary figures, a video, and a supplemental table. Fig. S1 contains data supporting Fig. 1; it shows the collapse of growth cones after stimulation with WIN in control or under metabolic inhibition. Fig. S2 contains data supporting Fig. 3; it shows a schema of the glycolytic enzymes and immunofluorescences at growth cone of all the enzymes of the payoff phase. Video 1 contains data supporting Fig. 3 A; it shows the dynamic of a growth cone and its retraction after WIN. Table S1 supports Tables 1 and 2; it contains the results of the MS analysis (sheet 1), the 450 putative proteins interacting with NMII (sheet 2), and the GO term analysis (sheet 3).

Materials availability

This study did not generate new unique reagents.

Lead contact

Further information should be directed to and will be fulfilled by the lead contact, Diana Zala (diana.zala@inserm.fr).

Data availability

The data underlying all figures and tables are available in the published article and its online supplemental material. This study did not generate/analyze datasets/code.

Acknowledgments

We thank Julie Nguyen from the NeurImag facility at Institut of Psychiatry and Neurosciences of Paris, France, for the neuronal

cultures and Erwan Boëdec from the Biochemistry and Biophysics facility for help with western blots at Institut of Psychiatry and Neurosciences of Paris. We thank Sandrine Moutel of the Recombinant Antibody Platform and TAb-IP Platform of Institut Curie for providing antibodies. We also thank the Proteomics facility of the Institut Jacques Monod, supported by the Région Ile-de-France, Université Paris Cité, and Centre National de la Recherche Scientifique, for assistance. We thank Derin Reha Ulusoy for preliminary experiments and Sonia Garel for scientific discussions.

This work was supported by a grant from DIM Cerveau et Pensé 2015 Neuroflux (D. Zala) and by a donation from Agilebio (R. Santos). R. Santos is a Centre National de la Recherche Scientifique researcher; L. Lokmane, Z. Lenkei, and D. Zala are Institut National de la Santé et de la Recherche Médicale researchers.

Author contributions: R. Santos conceptualized the study, designed, conducted and analyzed experiments, and wrote the paper. L. Lokmane conducted and analyzed experiments, and revised the paper. D. Ozdemir, C. Traoré, A. Agesillas, and C. Hakibilen conducted experiments. Z. Lenkei conceptualized and supervised the study, and revised the paper. D. Zala conceptualized and supervised the study, designed, conducted and analyzed experiments, and wrote the paper.

Disclosures: The authors declare no competing interests exist.

Submitted: 27 June 2022

Revised: 4 April 2023

Accepted: 2 October 2023

References

- Alam, M.S. 2018. Proximity ligation assay (PLA). *Curr. Protoc. Immunol.* 123: e58. <https://doi.org/10.1002/cpim.58>
- Amano, M., M. Nakayama, and K. Kaibuchi. 2010. Rho-kinase/ROCK: A key regulator of the cytoskeleton and cell polarity. *Cytoskeleton*. 67:545–554. <https://doi.org/10.1002/cm.20472>
- Amin, E., B.N. Dubey, S.-C. Zhang, L. Gremer, R. Dvorsky, J.M. Moll, M.S. Taha, L. Nagel-Steger, R.P. Piekorz, A.V. Somlyo, and M.R. Ahmadian. 2013. Rho-kinase: Regulation, (dys)function, and inhibition. *Biol. Chem.* 394:1399–1410. <https://doi.org/10.1515/hsz-2013-0181>
- Ashburner, M., C.A. Ball, J.A. Blake, D. Botstein, H. Butler, J.M. Cherry, A.P. Davis, K. Dolinski, S.S. Dwight, J.T. Eppig, et al. 2000. Gene ontology: Tool for the unification of biology. The Gene Ontology Consortium. *Nat. Genet.* 25:25–29. <https://doi.org/10.1038/75556>
- Backer, S., L. Lokmane, C. Landragin, M. Deck, S. Garel, and E. Bloch-Gallego. 2018. Trio GEF mediates RhoA activation downstream of Slit2 and

- coordinates telencephalic wiring. *Development*. 145:dev153692. <https://doi.org/10.1242/dev.153692>
- Begum, N., O.A. Sandu, M. Ito, S.M. Lohmann, and A. Smolenski. 2002. Active Rho kinase (ROK- α) associates with insulin receptor substrate-1 and inhibits insulin signaling in vascular smooth muscle cells. *J. Biol. Chem.* 277:6214–6222. <https://doi.org/10.1074/jbc.M110508200>
- Berg, J., Y.P. Hung, and G. Yellen. 2009. A genetically encoded fluorescent reporter of ATP:ADP ratio. *Nat. Methods*. 6:161–166. <https://doi.org/10.1038/nmeth.1288>
- Berghuis, P., A.M. Rajnicek, Y.M. Morozov, R.A. Ross, J. Mulder, G.M. Urbán, K. Monory, G. Marsicano, M. Matteoli, A. Canty, et al. 2007. Hardwiring the brain: Endocannabinoids shape neuronal connectivity. *Science*. 316:1212–1216. <https://doi.org/10.1126/science.1137406>
- Blockus, H., and A. Chédotal. 2016. Slit-Robo signaling. *Development*. 143:3037–3044. <https://doi.org/10.1242/dev.132829>
- Brown, J.A., R.B. Wysolmerski, and P.C. Bridgman. 2009. Dorsal root ganglion neurons react to semaphorin 3A application through a biphasic response that requires multiple myosin II isoforms. *Mol. Biol. Cell*. 20:1167–1179. <https://doi.org/10.1091/mbc.e08-01-0065>
- Cappello, S., C.R.J. Böhringer, M. Bergami, K.-K. Conzelmann, A. Ghanem, G.S. Tomassy, P. Arlotta, M. Mainardi, M. Allegra, M. Caleo, et al. 2012. A radial glia-specific role of RhoA in double cortex formation. *Neuron*. 73:911–924. <https://doi.org/10.1016/j.neuron.2011.12.030>
- Chédotal, A., and L.J. Richards. 2010. Wiring the brain: The biology of neuronal guidance. *Cold Spring Harb. Perspect. Biol.* 2:a001917. <https://doi.org/10.1101/cshperspect.a001917>
- Costa, B., and M. Colleoni. 2000. Changes in rat brain energetic metabolism after exposure to anandamide or Delta(9)-tetrahydrocannabinol. *Eur. J. Pharmacol.* 395:1–7. [https://doi.org/10.1016/s0014-2999\(00\)00170-9](https://doi.org/10.1016/s0014-2999(00)00170-9)
- Courchet, J., T.L. Lewis Jr., S. Lee, V. Courchet, D.-Y. Liou, S. Aizawa, and F. Polleux. 2013. Terminal axon branching is regulated by the LKB1-NUAK1 kinase pathway via presynaptic mitochondrial capture. *Cell*. 153:1510–1525. <https://doi.org/10.1016/j.cell.2013.05.021>
- Cowan, W.M., J.W. Fawcett, D.D. O'Leary, and B.B. Stanfield. 1984. Regressive events in neurogenesis. *Science*. 225:1258–1265. <https://doi.org/10.1126/science.6474175>
- Dastoor, Z., and J.-L. Dreyer. 2001. Potential role of nuclear translocation of glyceraldehyde-3-phosphate dehydrogenase in apoptosis and oxidative stress. *J. Cell Sci.* 114:1643–1653. <https://doi.org/10.1242/jcs.114.9.1643>
- Díaz-García, C.M., and G. Yellen. 2019. Neurons rely on glucose rather than astrocytic lactate during stimulation. *J. Neurosci. Res.* 97:883–889. <https://doi.org/10.1002/jnr.24374>
- Díaz-García, C.M., R. Mongeon, C. Lahmann, D. Koveal, H. Zucker, and G. Yellen. 2017. Neuronal stimulation triggers neuronal glycolysis and not lactate uptake. *Cell Metab.* 26:361–374.e4. <https://doi.org/10.1016/j.cmet.2017.06.021>
- Dumoulin, A., N.R. Zúñiga, and E.T. Stoekli. 2021. Axon guidance at the spinal cord midline-A live imaging perspective. *J. Comp. Neurol.* 529:2517–2538. <https://doi.org/10.1002/cne.25107>
- Engle, E.C. 2010. Human genetic disorders of axon guidance. *Cold Spring Harb. Perspect. Biol.* 2:a001784. <https://doi.org/10.1101/cshperspect.a001784>
- Fredriksson, S., M. Gullberg, J. Jarvius, C. Olsson, K. Pietras, S.M. Gustafsdóttir, A. Ostman, and U. Landegren. 2002. Protein detection using proximity-dependent DNA ligation assays. *Nat. Biotechnol.* 20:473–477. <https://doi.org/10.1038/nbt0502-473>
- Furukawa, N., P. Ongusaha, W.J. Jahng, K. Araki, C.S. Choi, H.-J. Kim, Y.H. Lee, K. Kaibuchi, B.B. Kahn, H. Masuzaki, et al. 2005. Role of Rho-kinase in regulation of insulin action and glucose homeostasis. *Cell Metab.* 2:119–129. <https://doi.org/10.1016/j.cmet.2005.06.011>
- Gaffuri, A.-L., D. Ladarre, and Z. Lenkei. 2012. Type-1 cannabinoid receptor signaling in neuronal development. *Pharmacology*. 90:19–39. <https://doi.org/10.1159/000339075>
- Gallo, G. 2006. RhoA-kinase coordinates F-actin organization and myosin II activity during semaphorin-3A-induced axon retraction. *J. Cell Sci.* 119:3413–3423. <https://doi.org/10.1242/jcs.03084>
- Gan, W.B., and J.W. Lichtman. 1998. Synaptic segregation at the developing neuromuscular junction. *Science*. 282:1508–1511. <https://doi.org/10.1126/science.282.5393.1508>
- Garrido-Casado, M., G. Asensio-Juárez, and M. Vicente-Manzanares. 2021. Nonmuscle myosin II regulation directs its multiple roles in cell migration and division. *Annu. Rev. Cell Dev. Biol.* 37:285–310. <https://doi.org/10.1146/annurev-cellbio-042721-105528>
- Geeves, M.A. 2016. Review: The ATPase mechanism of myosin and actomyosin. *Biopolymers*. 105:483–491. <https://doi.org/10.1002/bip.22853>
- Gene Ontology Consortium. 2021. The Gene Ontology resource: Enriching a Gold mine. *Nucleic Acids Res.* 49:D325–D334. <https://doi.org/10.1093/nar/gkaa1113>
- George, E.B., B.F. Schneider, R.J. Lasek, and M.J. Katz. 1988. Axonal shortening and the mechanisms of axonal motility. *Cell Motil. Cytoskeleton*. 9:48–59. <https://doi.org/10.1002/cm.970090106>
- Go, C.D., J.D.R. Knight, A. Rajasekharan, B. Rathod, G.G. Hesketh, K.T. Abe, J.-Y. Youn, P. Samavarchi-Tehrani, H. Zhang, L.Y. Zhu, et al. 2021. A proximity-dependent biotinylation map of a human cell. *Nature*. 595:120–124. <https://doi.org/10.1038/s41586-021-03592-2>
- Guy, A.T., and H. Kamiguchi. 2021. Lipids as new players in axon guidance and circuit development. *Curr. Opin. Neurobiol.* 66:22–29. <https://doi.org/10.1016/j.conb.2020.09.003>
- Havugimana, P.C., R.K. Goel, S. Phanse, A. Youssef, D. Padhorny, S. Kotelnikov, D. Kozakov, and A. Emili. 2022. Scalable multiplex co-fractionation/mass spectrometry platform for accelerated protein interactome discovery. *Nat. Commun.* 13:4043. <https://doi.org/10.1038/s41467-022-31809-z>
- Hebert-Chatelain, E., T. Desprez, R. Serrat, L. Bellocchio, E. Soria-Gomez, A. Busquets-Garcia, A.C. Pagano Zottola, A. Delamarre, A. Cannich, P. Vincent, et al. 2016. A cannabinoid link between mitochondria and memory. *Nature*. 539:555–559. <https://doi.org/10.1038/nature20127>
- Hinckelmann, M.-V., A. Virlogeux, C. Niehage, C. Poujol, D. Choquet, B. Hoflack, D. Zala, and F. Saudou. 2016. Self-propelling vesicles define glycolysis as the minimal energy machinery for neuronal transport. *Nat. Commun.* 7:13233. <https://doi.org/10.1038/ncomms13233>
- Ikemoto, A., D.G. Bole, and T. Ueda. 2003. Glycolysis and glutamate accumulation into synaptic vesicles. Role of glyceraldehyde phosphate dehydrogenase and 3-phosphoglycerate kinase. *J. Biol. Chem.* 278:5929–5940. <https://doi.org/10.1074/jbc.M211617200>
- Ishida, A., Y. Noda, and T. Ueda. 2009. Synaptic vesicle-bound pyruvate kinase can support vesicular glutamate uptake. *Neurochem. Res.* 34:807–818. <https://doi.org/10.1007/s10644-008-9833-3>
- Ivannikov, M.V., M. Sugimori, and R.R. Llinás. 2010. Calcium clearance and its energy requirements in cerebellar neurons. *Cell Calcium*. 47:507–513. <https://doi.org/10.1016/j.ceca.2010.04.004>
- Jiang, Y., Y. Wang, T. Wang, D.H. Hawke, Y. Zheng, X. Li, Q. Zhou, S. Majumder, E. Bi, D.X. Liu, et al. 2014. PKM2 phosphorylates MLC2 and regulates cytokinesis of tumour cells. *Nat. Commun.* 5:5566. <https://doi.org/10.1038/ncomms5566>
- Kaech, S., C.-F. Huang, and G. Banker. 2012. Long-term time-lapse imaging of developing hippocampal neurons in culture. *Cold Spring Harb. Protoc.* 2012:335–339. <https://doi.org/10.1101/pdb.prot068239>
- Ketschek, A., R. Sainath, S. Holland, and G. Gallo. 2021. The axonal glycolytic pathway contributes to sensory axon extension and growth cone dynamics. *J. Neurosci.* 41:6637–6651. <https://doi.org/10.1523/JNEUROSCI.0321-21.2021>
- Kim, Y., K.C. Vadodaria, Z. Lenkei, T. Kato, F.H. Gage, M.C. Marchetto, and R. Santos. 2019. Mitochondria, metabolism, and redox mechanisms in psychiatric disorders. *Antioxid. Redox Signal.* 31:275–317. <https://doi.org/10.1089/ars.2018.7606>
- Knoll, H.R., and J.L. Walsh. 1992. Association of glycolytic enzymes with the cytoskeleton. *Curr. Top. Cell. Regul.* 33:15–30. <https://doi.org/10.1016/b978-0-12-152833-1.50007-1>
- Lautarescu, A., D. Pecheva, C. Nosarti, J. Nihouarn, H. Zhang, S. Victor, M. Craig, A.D. Edwards, and S.J. Counsell. 2020. Maternal prenatal stress is associated with altered uncinate fasciculus microstructure in premature neonates. *Biol. Psychiatry*. 87:559–569. <https://doi.org/10.1016/j.biopsych.2019.08.010>
- Leterrier, C., J. Lainé, M. Darmon, H. Boudin, J. Rossier, and Z. Lenkei. 2006. Constitutive activation drives compartment-selective endocytosis and axonal targeting of type 1 cannabinoid receptors. *J. Neurosci.* 26:3141–3153. <https://doi.org/10.1523/JNEUROSCI.5437-05.2006>
- Lokmane, L., and S. Garel. 2014. Map transfer from the thalamus to the neocortex: Inputs from the barrel field. *Semin. Cell Dev. Biol.* 35:147–155. <https://doi.org/10.1016/j.semcdb.2014.07.005>
- Luo, L., and D.D.M. O'Leary. 2005. Axon retraction and degeneration in development and disease. *Annu. Rev. Neurosci.* 28:127–156. <https://doi.org/10.1146/annurev.neuro.28.061604.135632>
- Lyon, A.S., W.B. Peeples, and M.K. Rosen. 2021. A framework for understanding the functions of biomolecular condensates across scales. *Nat. Rev. Mol. Cell Biol.* 22:215–235. <https://doi.org/10.1038/s41580-020-00303-z>
- Maccarrone, M., M. Guzmán, K. Mackie, P. Doherty, and T. Harkany. 2014. Programming of neural cells by (endo)cannabinoids: From physiological

- rules to emerging therapies. *Nat. Rev. Neurosci.* 15:786–801. <https://doi.org/10.1038/nrn3846>
- Masters, C. 1984. Interactions between glycolytic enzymes and components of the cytomatrix. *J. Cell Biol.* 99:222s–225s. <https://doi.org/10.1083/jcb.99.1.222s>
- McCormick, L.E., and S.L. Gup-ton. 2020. Mechanistic advances in axon pathfinding. *Curr. Opin. Cell Biol.* 63:11–19. <https://doi.org/10.1016/j.ccb.2019.12.003>
- Meyer, D.J., C.M. Díaz-García, N. Nathwani, M. Rahman, and G. Yellen. 2022. The Na⁺/K⁺ pump dominates control of glycolysis in hippocampal dentate granule cells. *Elife*. 11:e81645. <https://doi.org/10.7554/eLife.81645>
- Mi, H., A. Muruganujan, D. Ebert, X. Huang, and P.D. Thomas. 2019. PANTHER version 14: More genomes, a new PANTHER GO-slim and improvements in enrichment analysis tools. *Nucleic Acids Res.* 47: D419–D426. <https://doi.org/10.1093/nar/gky1038>
- Miller, K.E., and D.M. Suter. 2018. An integrated cytoskeletal model of neurite outgrowth. *Front. Cell. Neurosci.* 12:447. <https://doi.org/10.3389/fncel.2018.00447>
- Mulder, J., T. Aguado, E. Keimpema, K. Barabás, C.J. Ballester Rosado, L. Nguyen, K. Monory, G. Marsicano, V. Di Marzo, Y.L. Hurd, et al. 2008. Endocannabinoid signaling controls pyramidal cell specification and long-range axon patterning. *Proc. Natl. Acad. Sci. USA*. 105:8760–8765. <https://doi.org/10.1073/pnas.0803545105>
- Murray, A., A. Naeem, S.H. Barnes, U. Drescher, and S. Guthrie. 2010. Slit and Netrin-1 guide cranial motor axon pathfinding via Rho-kinase, myosin light chain kinase and myosin II. *Neural Dev.* 5:16. <https://doi.org/10.1186/1749-8104-5-16>
- Narumiya, S., and D. Thumkeo. 2018. Rho signaling research: History, current status and future directions. *FEBS Lett.* 592:1763–1776. <https://doi.org/10.1002/1873-3468.13087>
- Obara, Y., S. Ueno, Y. Yanagihata, and N. Nakahata. 2011. Lysophosphatidylinositol causes neurite retraction via GPR55, G13 and RhoA in PC12 cells. *PLoS One*. 6:e24284. <https://doi.org/10.1371/journal.pone.0024284>
- Oyarzábal, A., U. Musokhranova, B. Lf, and A. García-Cazorla. 2021. Energy metabolism in childhood neurodevelopmental disorders. *EBioMedicine*. 69:103474. <https://doi.org/10.1016/j.ebiom.2021.103474>
- Park, J.S., C.J. Burckhardt, R. Lazcano, L.M. Solis, T. Isogai, L. Li, C.S. Chen, B. Gao, J.D. Minna, R. Bachoo, et al. 2020. Mechanical regulation of glycolysis via cytoskeleton architecture. *Nature*. 578:621–626. <https://doi.org/10.1038/s41586-020-1998-1>
- Pease, S.E., and R.A. Segal. 2014. Preserve and protect: Maintaining axons within functional circuits. *Trends Neurosci.* 37:572–582. <https://doi.org/10.1016/j.tins.2014.07.007>
- Peyrin, J.-M., B. Deleglise, L. Saias, M. Vignes, P. Gougis, S. Magnifico, S. Betuing, M. Pietri, J. Caboche, P. Vanhoutte, et al. 2011. Axon diodes for the reconstruction of oriented neuronal networks in microfluidic chambers. *Lab Chip*. 11:3663–3673. <https://doi.org/10.1039/c1lc20014c>
- Pfeiffer, T., S. Schuster, and S. Bonhoeffer. 2001. Cooperation and competition in the evolution of ATP-producing pathways. *Science*. 292:504–507. <https://doi.org/10.1126/science.1058079>
- Quarta, S., M. Camprubi-Robles, R. Schweigreiter, D. Matusica, R.V. Haberman, R.L. Proia, C.E. Bandtlow, A. Ferrer-Montiel, and M. Kress. 2017. Sphingosine-1-Phosphate and the S1P₃ receptor initiate neuronal retraction via RhoA/ROCK associated with CRMP2 phosphorylation. *Front. Mol. Neurosci.* 10:317. <https://doi.org/10.3389/fnmol.2017.00317>
- Rasmussen, J.M., A.M. Graham, S. Entringer, J.H. Gilmore, M. Styner, D.A. Fair, P.D. Wadhwa, and C. Buss. 2019. Maternal Interleukin-6 concentration during pregnancy is associated with variation in frontolimbic white matter and cognitive development in early life. *Neuroimage*. 185: 825–835. <https://doi.org/10.1016/j.neuroimage.2018.04.020>
- Riedel, J., A.H. Crevenna, K. Kessenbrock, J.H. Yu, D. Neukirchen, M. Bista, F. Bradke, D. Jenne, T.A. Holak, Z. Werb, et al. 2008. Lifeact: A versatile marker to visualize F-actin. *Nat. Methods*. 5:605–607. <https://doi.org/10.1038/nmeth.1220>
- Roland, A.B., A. Ricobaraza, D. Carrel, B.M. Jordan, F. Rico, A. Simon, M. Humbert-Claude, J. Ferrier, M.H. McFadden, S. Scheuring, and Z. Lenkei. 2014. Cannabinoid-induced actomyosin contractility shapes neuronal morphology and growth. *Elife*. 3:e03159. <https://doi.org/10.7554/eLife.03159>
- Saez, T.M.M., I. Fernandez Bessone, M.S. Rodriguez, M. Alloati, M.G. Otero, L.E. Cromberg, V.M. Pozo Devoto, G. Oubiña, L. Sosa, M.G. Buffone, et al. 2020. Kinesin-1-mediated axonal transport of CB1 receptors is required for cannabinoid-dependent axonal growth and guidance. *Development*. 147:dev184069. <https://doi.org/10.1242/dev.184069>
- Salvi, A.M., J.L. Bays, S.R. Mackin, R.-M. Mege, and K.A. DeMali. 2021. Ankyrin G organizes membrane components to promote coupling of cell mechanics and glucose uptake. *Nat. Cell Biol.* 23:457–466. <https://doi.org/10.1038/s41556-021-00677-y>
- Schindelin, J., I. Arganda-Carreras, E. Frise, V. Kaynig, M. Longair, T. Pietzsch, S. Preibisch, C. Rueden, S. Saalfeld, B. Schmid, et al. 2012. Fiji: An open-source platform for biological-image analysis. *Nat. Methods*. 9: 676–682. <https://doi.org/10.1038/nmeth.2019>
- Schmitz, H.-D., and J. Bereiter-Hahn. 2002. Glyceraldehyde-3-phosphate dehydrogenase associates with actin filaments in serum deprived NIH 3T3 cells only. *Cell Biol. Int.* 26:155–164. <https://doi.org/10.1006/cbir.2001.0819>
- Seiradake, E., E.Y. Jones, and R. Klein. 2016. Structural perspectives on axon guidance. *Annu. Rev. Cell Dev. Biol.* 32:577–608. <https://doi.org/10.1146/annurev-cellbio-111315-125008>
- Shamah, S.M., M.Z. Lin, J.L. Goldberg, S. Estrach, M. Sahin, L. Hu, M. Bazalakova, R.L. Neve, G. Corfas, A. Debant, and M.E. Greenberg. 2001. EphA receptors regulate growth cone dynamics through the novel guanine nucleotide exchange factor ephexin. *Cell*. 105:233–244. [https://doi.org/10.1016/s0092-8674\(01\)00314-2](https://doi.org/10.1016/s0092-8674(01)00314-2)
- Shearwin, K., C. Nanhua, and C. Masters. 1990. Interactions between glycolytic enzymes and cytoskeletal structure—the influence of ionic strength and molecular crowding. *Biochem. Int.* 21:53–60.
- Sirover, M.A. 2020. Moonlighting glyceraldehyde-3-phosphate dehydrogenase: Posttranslational modification, protein and nucleic acid interactions in normal cells and in human pathology. *Crit. Rev. Biochem. Mol. Biol.* 55:354–371. <https://doi.org/10.1080/10409238.2020.1787325>
- Sirover, M.A. 2021. The role of posttranslational modification in moonlighting glyceraldehyde-3-phosphate dehydrogenase structure and function. *Amino Acids*. 53:507–515. <https://doi.org/10.1007/s00726-021-02959-z>
- Smith, G.M., and G. Gallo. 2018. The role of mitochondria in axon development and regeneration. *Dev. Neurobiol.* 78:221–237. <https://doi.org/10.1002/dneu.22546>
- Sweetlove, L.J., and A.R. Fernie. 2018. The role of dynamic enzyme assemblies and substrate channelling in metabolic regulation. *Nat. Commun.* 9:2136. <https://doi.org/10.1038/s41467-018-04543-8>
- Takeuchi, S., H. Katoh, and M. Negishi. 2015. Eph/ephrin reverse signalling induces axonal retraction through RhoA/ROCK pathway. *J. Biochem.* 158:245–252. <https://doi.org/10.1093/jb/mvv042>
- Taylor, A.M., M. Blurton-Jones, S.W. Rhee, D.H. Cribbs, C.W. Cotman, and N.L. Jeon. 2005. A microfluidic culture platform for CNS axonal injury, regeneration and transport. *Nat. Methods*. 2:599–605. <https://doi.org/10.1038/nmeth777>
- Tortoriello, G., C.V. Morris, A. Alpar, J. Fuzik, S.L. Shirran, D. Calvigioni, E. Keimpema, C.H. Botting, K. Reinecke, T. Herdegen, et al. 2014. Miswiring the brain: Δ9-tetrahydrocannabinol disrupts cortical development by inducing an SCG10/stathmin-2 degradation pathway. *EMBO J.* 33:668–685. <https://doi.org/10.1002/emboj.201386035>
- Van Battum, E.Y., S. Brignani, and R.J. Pasterkamp. 2015. Axon guidance proteins in neurological disorders. *Lancet Neurol.* 14:532–546. [https://doi.org/10.1016/S1474-4422\(14\)70257-1](https://doi.org/10.1016/S1474-4422(14)70257-1)
- Wahl, S., H. Barth, T. Ciossek, K. Aktories, and B.K. Mueller. 2000. Ephrin-A5 induces collapse of growth cones by activating Rho and Rho kinase. *J. Cell Biol.* 149:263–270. <https://doi.org/10.1083/jcb.149.2.263>
- Waingeh, V.F., C.D. Gustafson, E.I. Kozliak, S.L. Lowe, H.R. Knull, and K.A. Thomasson. 2006. Glycolytic enzyme interactions with yeast and skeletal muscle F-actin. *Biophys. J.* 90:1371–1384. <https://doi.org/10.1529/biophysj.105.070052>
- Wen, Z., and J.Q. Zheng. 2006. Directional guidance of nerve growth cones. *Curr. Opin. Neurobiol.* 16:52–58. <https://doi.org/10.1016/j.conb.2005.12.005>
- Wu, C.-S., J. Zhu, J. Wager-Miller, S. Wang, D. O’Leary, K. Monory, B. Lutz, K. Mackie, and H.-C. Lu. 2010. Requirement of cannabinoid CB(1) receptors in cortical pyramidal neurons for appropriate development of corticothalamic and thalamocortical projections. *Eur. J. Neurosci.* 32: 693–706. <https://doi.org/10.1111/j.1460-9568.2010.07337.x>
- Wu, D., D.L. Harrison, T. Szasz, C.-F. Yeh, T.-P. Shentu, A. Meliton, R.-T. Huang, Z. Zhou, G.M. Mutlu, J. Huang, and Y. Fang. 2021. Single-cell metabolic imaging reveals a SLC2A3-dependent glycolytic burst in motile endothelial cells. *Nat. Metab.* 3:714–727. <https://doi.org/10.1038/s42255-021-00390-y>
- Wylie, S.R., and P.D. Chantler. 2003. Myosin IIA drives neurite retraction. *Mol. Biol. Cell*. 14:4654–4666. <https://doi.org/10.1091/mbc.e03-03-0187>
- Yang, J.-Q., K.W. Kalim, Y. Li, S. Zhang, A. Hinge, M.-D. Filippi, Y. Zheng, and F. Guo. 2016. RhoA orchestrates glycolysis for TH2 cell differentiation

- and allergic airway inflammation. *J. Allergy Clin. Immunol.* 137: 231–245.e4. <https://doi.org/10.1016/j.jaci.2015.05.004>
- Ye, X., Y. Qiu, Y. Gao, D. Wan, and H. Zhu. 2019. A subtle network mediating axon guidance: Intrinsic dynamic structure of growth cone, attractive and repulsive molecular cues, and the intermediate role of signaling pathways. *Neural Plast.* 2019:1719829. <https://doi.org/10.1155/2019/1719829>
- Yellen, G. 2018. Fueling thought: Management of glycolysis and oxidative phosphorylation in neuronal metabolism. *J. Cell Biol.* 217:2235–2246. <https://doi.org/10.1083/jcb.201803152>
- Zala, D., M.-V. Hinckelmann, H. Yu, M.M. Lyra da Cunha, G. Liot, F.P. Cordelières, S. Marco, and F. Saudou. 2013. Vesicular glycolysis provides on-board energy for fast axonal transport. *Cell.* 152:479–491. <https://doi.org/10.1016/j.cell.2012.12.029>
- Zala, D., U. Schlattner, T. Desvignes, J. Bobe, A. Roux, P. Chavrier, and M. Boissan. 2017. The advantage of channeling nucleotides for very processive functions. *Fl000Res.* 6:724. <https://doi.org/10.12688/fl000research.11561.2>
- Zhang, X.-F., A.W. Schaefer, D.T. Burnette, V.T. Schoonderwoert, and P. Forscher. 2003. Rho-dependent contractile responses in the neuronal growth cone are independent of classical peripheral retrograde actin flow. *Neuron.* 40:931–944. [https://doi.org/10.1016/s0896-6273\(03\)00754-2](https://doi.org/10.1016/s0896-6273(03)00754-2)
- Zhang, Y., and A.R. Fernie. 2021. Stable and temporary enzyme complexes and metabolons involved in energy and redox metabolism. *Antioxid. Redox Signal.* 35:788–807. <https://doi.org/10.1089/ars.2019.7981>

Supplemental material

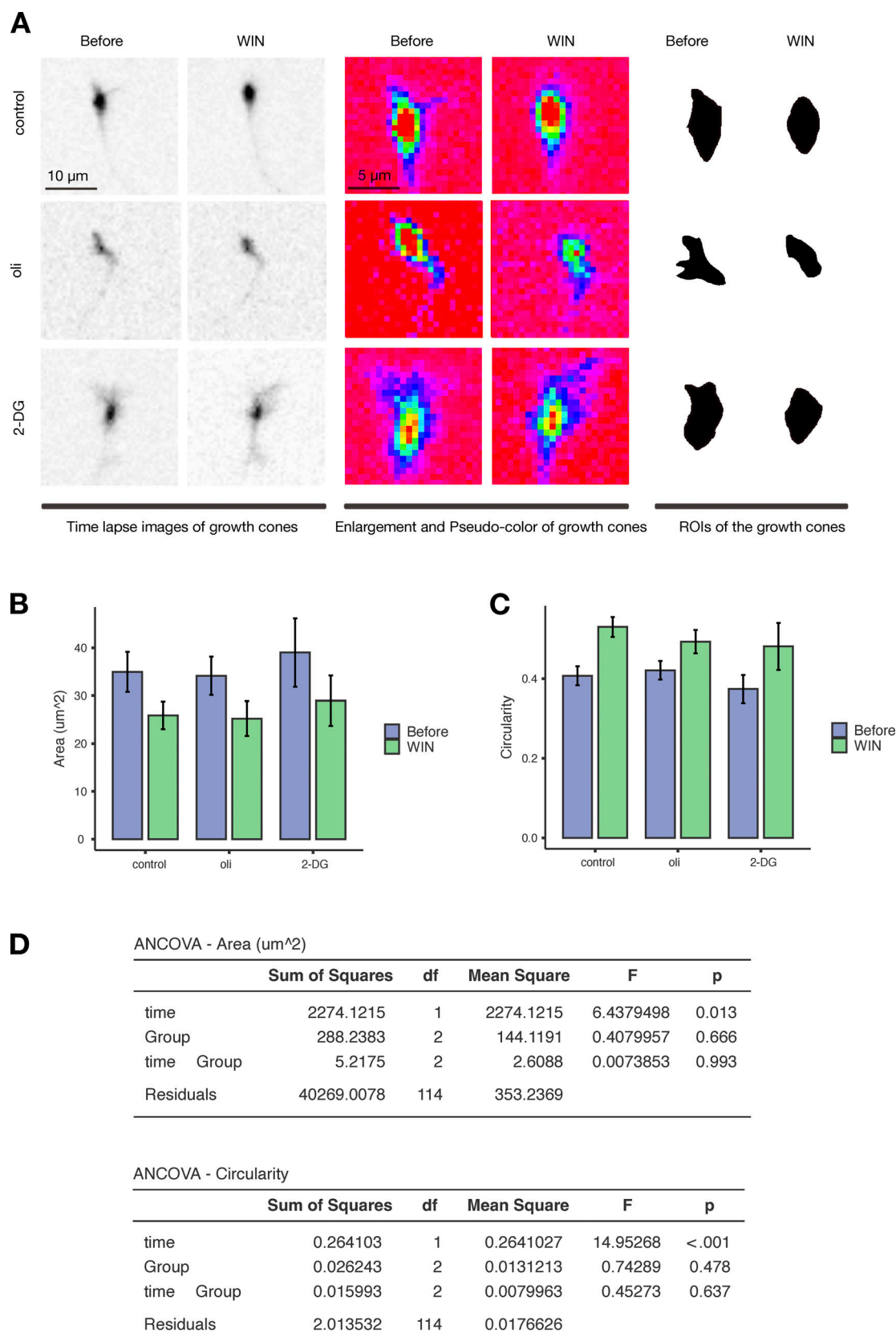


Figure S1. **Growth cone collapse quantification.** (Related to Fig. 1.) (A) Left, the shape of the growth cones before and after WIN-induced retraction under metabolic inhibition (oligomycin [oli], 2DG, or control). Center, enlargement of the growth cones with pseudocolor allowing the drawing of the region of interest (ROI, right). (B and C) Bar graphs with \pm SEM of ROI calculated area (B and C) circularity. The formula for circularity is $4\pi (\text{area}/\text{perimeter}^2)$, and a value of 1.0 indicates a perfect circle (imagej). (D) Statistical analyses (df: degrees of freedom, F: ANOVA F-value, p: probability of a type I error).

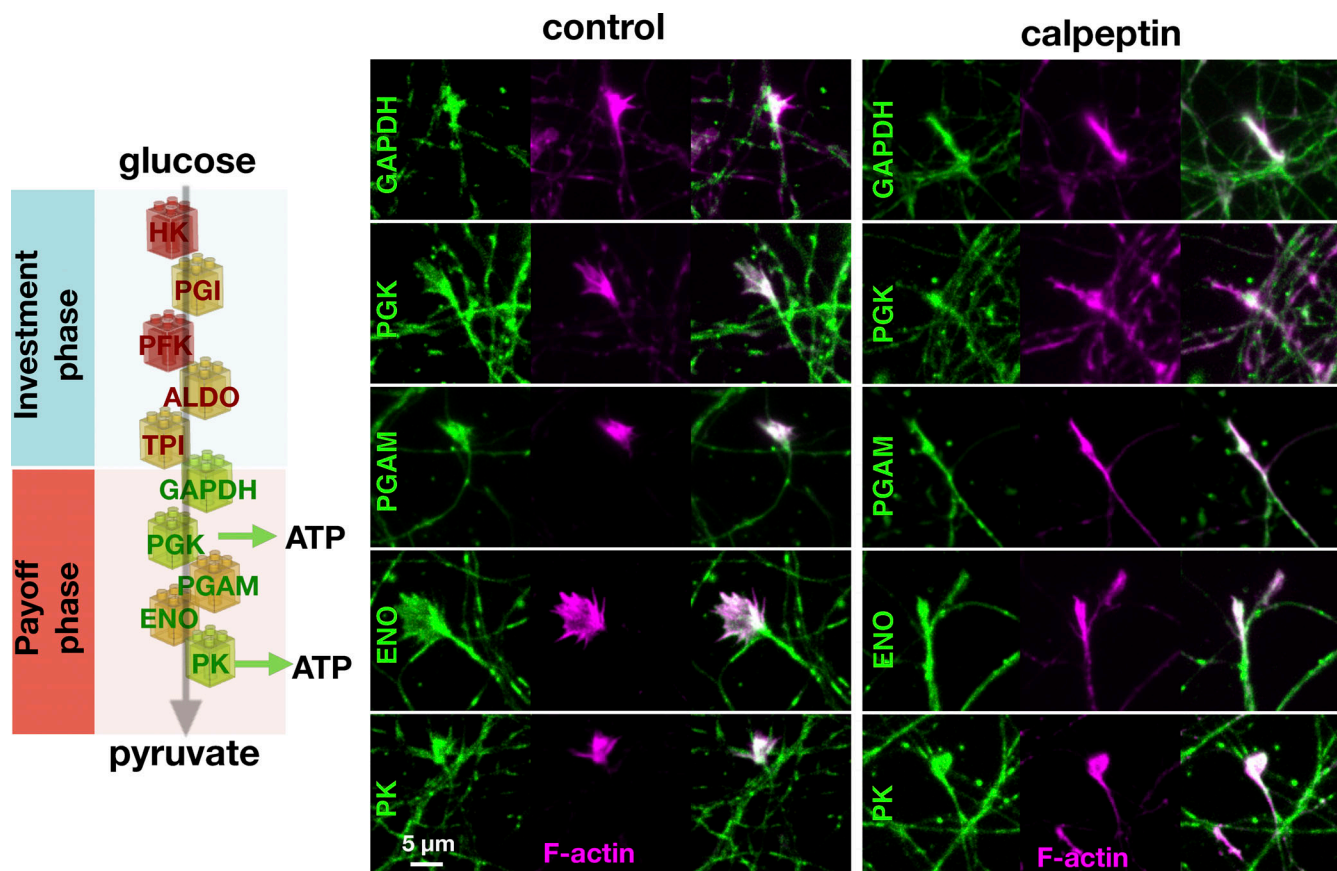


Figure S2. **The five glycolytic payoff phase enzymes are located at the growth cone and near the shaft during axonal retraction.** (Related to Fig. 3.) Schematic representation of the steps of glycolysis split into investment and payoff phases. In green, immunostaining of growth cones for each of the five glycolytic enzymes of the payoff phase in hippocampal cultures treated for 5 min with control (DMSO) or 0.2 U/ml calpeptin. Growth cones are recognized by their characteristic morphology with the phalloidin staining in magenta. Note the collapse of growth cones by calpeptin as compared to control. HK, hexokinase; PGI, glucose-6-phosphate isomerase; PFK, phosphofructokinase; ALDO, aldolase; PGAM, phosphoglycerate mutase; ENO, enolase.

Video 1. **Time-lapse of a growth cone of hippocampal neurons expressing GAPDH-eGFP (green), LifeAct-mCherry (red), and CB1-CFP (blue).** (Related to Fig. 3.) At the bottom is shown the overlay of the three channels. At 24 min, 100 nM WIN was injected to induce axonal retraction (7 frames/s).

Provided online is Table S1, which shows MS analysis of NMII and eGFP coimmunoprecipitation samples.